Graduate School Form
30 Updated 12/26/2015

PURDUE UNIVERSITY
GRADUATE SCHOOL
Thesis/Dissertation Acceptance

This is to certify that the thesis/dissertation prepared

By Luize Scalco de Vasconcelos

Entitled

HIGH-THROUGHPUT MECHANICAL CHARACTERIZATION METHODS FOR COMPOSITE ELECTRODES AND IN-SITU ANALYSIS OF LI-ION BATTERIES

For the degree of Master of Science in Mechanical Engineering

Is approved by the final examining committee:

Kejie Zhao
Chair

Liang Pan

Ramiro Edwin Garcia

To the best of my knowledge and as understood by the student in the Thesis/Dissertation Agreement, Publication Delay, and Certification Disclaimer (Graduate School Form 32), this thesis/dissertation adheres to the provisions of Purdue University's "Policy of Integrity in Research" and the use of copyright material.

Approved by Major Professor(s): Kejie Zhao

Approved by: Jay P. Gore 7/7/2016

Head of the Departmental Graduate Program Date

HIGH-THROUGHPUT MECHANICAL CHARACTERIZATION METHODS FOR COMPOSITE ELECTRODES AND IN-SITU ANALYSIS OF LI-ION BATTERIES

A Thesis

Submitted to the Faculty

of

Purdue University

by

Luize Scalco de Vasconcelos

In Partial Fulfillment of the

Requirements for the Degree

of

Master of Science in Mechanical Engineering

August 2016

Purdue University

West Lafayette, Indiana

ACKNOWLEDGEMENTS

First and foremost, I would like to express my sincere gratitude to my advisor, Prof. Kejie Zhao, for providing me his full support and trust during this time at Purdue. His genuine concern with the professional development and well-being of each and every student in our group, truly make us feel as part of a family. I bear a true appreciation for his guiding and encouraging us to pursue new challenges and develop the necessary skills to become well-rounded researchers.

I am also very fortunate to have worked in a group with such talented and cordial individuals. I would like to especially thank my colleague, Rong Xu, that as the first student in the group, has dedicated endless hours to training and helping the others. To my colleagues, who make my day exciting and productive, a sincere thank you!

I am grateful to the professors who participated in my education in the course of these two years. A special thanks to my committee members, Prof. Liang Pan and Prof. Edwin García, for the constructive and insightful comments on my thesis work. I would also like to thank Prof. Edwin García for his advice and availability to enlighten me on the fundamentals of rechargeable batteries.

I am extremely thankful to my career mentor, Mark Lamontia, for his everlasting friendship and guidance on every step of my academic endeavors. He has taught me precious lessons that I will carry for my lifetime.

Finally, I would like to thank all of my friends who have become my support system away from my native country. Most dearly, I would like to thank Vinícius for his companionship and my loving family Amilton, Mary and Daniele for the care and for being my inspiration.

I appreciate the financial support from the CAPES Foundation, Ministry of Education of Brazil, under grant 88888.075986/2013-00.

TABLE OF CONTENTS

Page

LIST OF TABLES

LIST OF FIGURES

Figure Page

Figure Page

ABSTRACT

Scalco de Vasconcelos, Luize. M.S.M.E., Purdue University, August 2016. High-Throughput Mechanical Characterization Methods for Composite Electrodes and In-Situ Analysis of Li-ion Batteries. Major Professor: Kejie Zhao.

Electrodes in commercial rechargeable batteries are microscopically heterogeneous materials. The constituents often have large variation in their mechanical properties, making the characterization process a challenging task. In addition, the mechanical properties and mechanical behaviors of electrodes are closely coupled with the electrochemical processes of lithium insertion and extraction. There is an urgent need to develop an experimental platform to characterize the chemomechanical response of electrodes under the in-situ conditions of charge and discharge.

In the first part of this thesis, instrumented grid indentation is employed to determine the elastic modulus and hardness of the constituent phases of a composite cathode. The approach relies on an array of indentations and statistical analysis of the experimental output. The statistically interpreted properties of the active particles and matrix are further validated through indentation at selected sites. The combinatory technique of grid indentation and statistical deconvolution is demonstrated to be a fast and reliable route to quantify the mechanical properties of composite electrodes.

In the second part of work, a nanoindenter, a liquid cell, and an electrochemical station are integrated into an inert gas filled glovebox. The developed experimental

platform makes it possible to perform mechanical tests of thin film electrodes during in-situ charge and discharge cycles and to monitor the evolution of the mechanical properties as a function of the state of charge. The technique overcomes practical issues related with environment requirements and instrument limitations, and enables comprehensive and consistent data acquisition. Furthermore, the procedure allows experiments to be carried out in a considerably shorter time than existing methods. In a preliminary study, this technique is applied to the in-situ characterization of silicon thin film and it is validated against the literature results.

Overall, the thesis work focuses on the mechanical characterization, both ex-situ and in-situ, of electrodes in Li-ion batteries. The developed methodology and experimental platform are significant toward the complete understanding of the chemomechanical behaviors of high-performance batteries.

1. INTRODUCTION

1.1 Basics of Li-ion batteries

This chapter starts by describing the working principles of Li-ion batteries (LIBs), its main components, and various mechanisms of degradation. Then it presents an overview of current techniques for mechanical characterization of materials in the field of research of energy materials. Finally, it outlines the structure of the thesis.

1.1.1 Working principles

The term electrochemical system refers to devices that can convert energy between two forms, chemical and electrical. An electrochemical cell is composed of three main components: a positive and a negative electrode separated by an electrolyte, as illustrated in Figure 1.1. The electrodes are electronically conductive, whereas the electrolyte can conduct ions, but block the movement of free electrons. The difference in the electrochemical potential of the two electrodes drives ions across the ionic conductive electrolyte, while electrons can only move through an external circuit connecting the two electrodes, either doing work or requiring work in the process. This ion and electron movement during charge and discharge is illustrated in Figure 1.1 for an Li-ion battery.

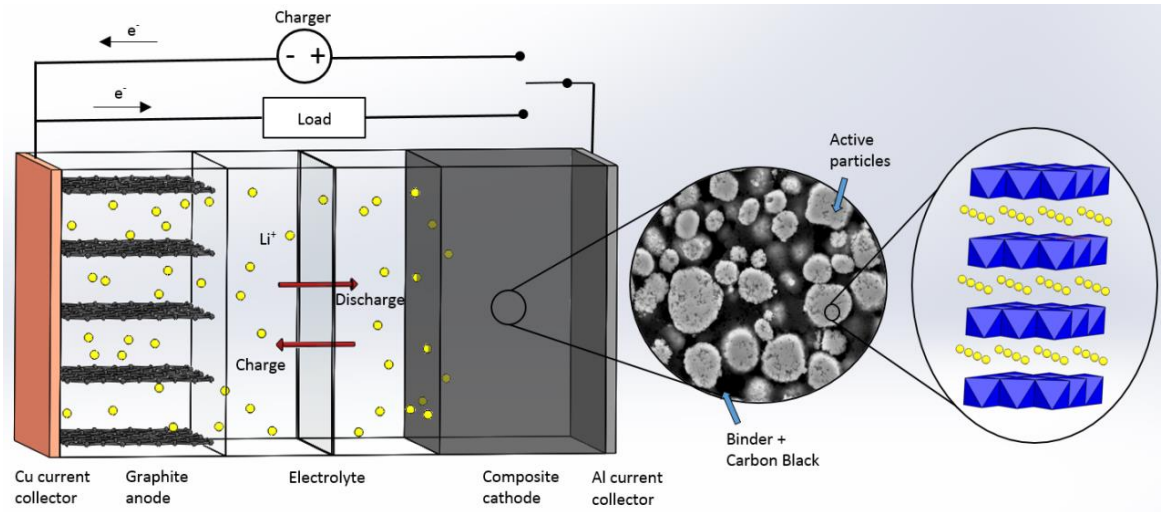

Figure 1.1. Working principle and major components of a Li-ion battery.

Major properties of electrochemical cells follow the thermodynamic and kinetic formulations for chemical reactions [1]. The thermodynamic properties of a material can be related to those of its constituents i through the concept of the chemical potential of an individual species as follows μ_i [2]:

$$\mu_i = \left(\frac{\partial G}{\partial n_i}\right)_{\substack{T,p,n_j \\ i \neq j}}, \tag{1.1}$$

where G is the Gibbs free energy, n_i is number of moles of species i, n_j is the number of moles of all species except for i, T is temperature and p is pressure. In an electrochemical system, the electrochemical potential $\bar{\mu}$ for a species i with a charge z_i in a phase α is defined as [3]:

$$\bar{\mu}_i^\alpha = \mu_i^\alpha + z_i F \phi^\alpha, \tag{1.2}$$

where F is the Faraday constant. Under equilibrium, the electrochemical potential between the species i in the α phase and the same species i in the β phase is balanced by

the voltage shift and the chemical potential of each phase. Thus, the voltage or electrical potential difference $\Delta\phi$ is given by [4]:

$$\bar{\mu}_i^{\alpha} = \bar{\mu}_i^{\beta} \rightarrow \Delta\phi^{\alpha\rightarrow\beta} = \frac{\Delta\mu_i^{\alpha\rightarrow\beta}}{z_i F} \tag{1.3}$$

Thermodynamics describe reactions at equilibrium, however, when current is drawn from a cell at an appreciable rate, there are a number of resistances related with kinetic limitations that cause the voltage to drop. The difference between the equilibrium voltage and observed voltage is often referred as the overpotential and can be grouped into three categories: activation, concentration, and ohmic [5]. The activation overpotential, also called activation polarization, is related with the kinetics of charge transfer at the interface of the electrode and electrolyte, while the concentration overpotential is caused by mass transport limitations. Finally, the ohmic overpotential is tied to the cell design through the resistance of its components and contacts [1]. All the overpotentials represent dissipative losses that increase in magnitude with an increase in the current density.

1.1.2 Electrode

In commercial batteries both the cathode and anode are composites of high heterogeneity at the nano- to microscale, consisting of active particles, a matrix composed of polymer binders and additives, and pores filled with the electrolyte. The active particles react with Li. Polymeric binders physically hold the active materials together. Conductive agents such as carbon black are added to enhance the electronic conductivity so that electrons can be transported to the active material. Moreover, sufficient porosity exists in the matrix to allow the liquid electrolyte to penetrate the matrix and transport ions to the

reacting sites. Electrode materials are coated on current collectors. The current collector material is selected according to its electrochemical stability window. The electrochemical stability of copper at low potentials makes it suitable as the anode current collector. Although aluminum is not electrochemically stable at high potentials, it is stabilized by a passivation layer formed from electrolyte degradation products and therefore is often used as the cathode current collector [6].

1.1.3 Electrolyte and SEI layer

The primary function of the electrolyte solution is to allow ion transport between cathode and anode. In practice, it must show a number of physicochemical properties in addition to good ionic conductivity, such as thermal stability, chemical stability, electrochemical windows covering operation voltages, stable formation of SEI layer, and minimum parasitic reactions [7].

Commercial electrolytes for Li-ion batteries are usually composed of lithium hexafluorophosphate ($LiPF_6$) salt dissolved in a nonaqueous solution of organic carbonates. A mixture of linear carbonates and cyclic carbonates is commonly used to take advantage of their dissimilar properties [7]. For example, ethylene carbonate (EC) assists in the stable formation of a passivating layer, but it has the drawback of having high melting point (34°C). Therefore, it requires the addition of co-solvents such as diethyl carbonate (DEC) and dimethyl carbonate (DMC) to be in the liquid state at ambient temperature [8]. Propylene carbonate (PC) has a wide liquid temperature range, however, it suffers from solvent decomposition on the anode surface, which causes electrode disintegration and delamination from current collector [8].

Numerous studies have been carried out to investigate the influence of the solvent ratios, salt concentration and additives on electrochemical performace [9] [10] [11]. Work by Petibon et al. [12] found evidence that increasing $LiPF_6$ concentration can minimize impedance growth when using certain additives, while the same phenomenon is not observed in the same test conditions without these additives. Therefore, how different variables affect electrochemical degradation is specific to each electrode/electrolyte combination and operation conditions used.

Electrolyte solvents are unstable at the operation potentials of Li-ion batteries and tend to reduce and oxidize on the surface of the negative and positive electrodes, respectively [13]. The products of these reactions form a protective interface layer between electrolyte and electrode named Solid-Electrolyte Interface (SEI). This layer limits further decomposition of the electrolyte by minimizing electronic conductivity, while still allowing lithium ion transport [14]. Ideally, the SEI would completely block electronic conductivity, while still allowing lithium ions to reversibly diffuse between the anode and cathode with no additional capacity fade. In practice, however, the SEI may continue to build-up resulting in a gradual capacity fade as it thickens. In addition to providing electronic insulation and high Li ion conductivity, the SEI must strongly adhere to active material and be sufficiently elastic and flexible to accommodate volumetric expansion of the active material, as well as be composed of insoluble passivating agents [15].

1.2 Failure of Li-ion batteries

Recent interest in alternative energy sources has led to stricter life and energy density requirements for energy storage systems. Electric/hybrid electric vehicles, for

example, require battery life up to 15 years [13]. Hence, understanding degradation mechanisms have become increasingly important and attracted numerous experimental and modeling studies [16] [17] [18].

Aging and failure in LIBs are caused by a number of complex and interrelated processes which, in many cases, are still not completely understood [13]. How degradation evolves depend on a variety of factors, including operating conditions such as cut-off voltages, operating temperature, and cycling rate. For example, high operating voltage and high temperature lead to premature deterioration of LIB state-of-health by, respectively, favoring and accelerating phase transitions and formation surface films [19]. Electrode composition and cut-off voltages can be tuned up for better capacity retention [20].

A summary of the most common degradation mechanisms in Li-ion batteries are illustrated in Figure 1.2 by Birkl [21].

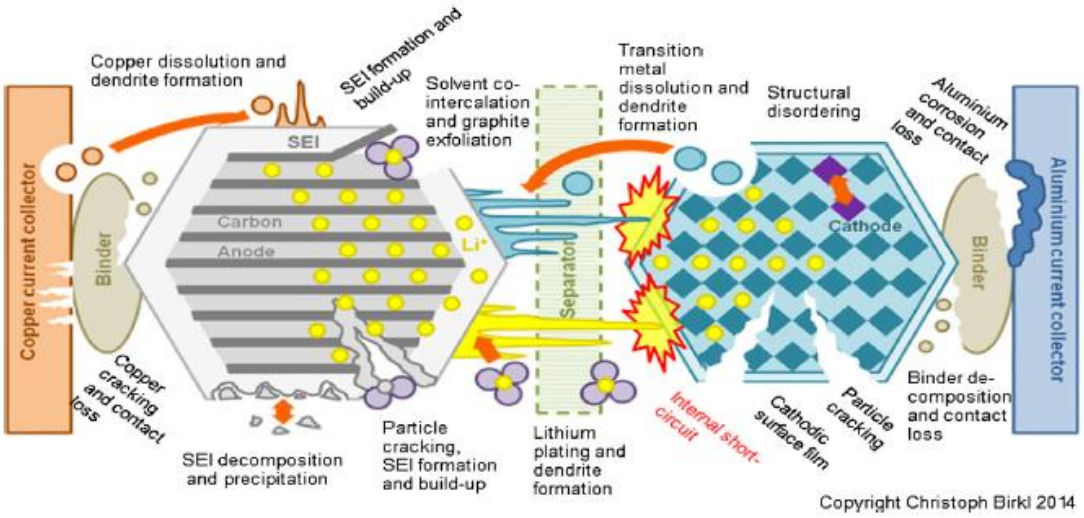

Figure 1.2. Illustration of common degradation mechanisms in Li-ion batteries [21].

Ultimately, degradation manifests as either voltage decay or capacity loss [13]. Voltage decay is a result of the impedance increase caused by loss of electron conduction

path and SEI layer growth, while capacity loss is mostly caused by electrode disintegration, material deterioration, and loss of free lithium [22].

1.2.1 Mechanical degradation

This worked focused on the degradation aspects related to structural stability of LIBs electrodes. Mechanical stability is one of the key criteria for the selection of electrodes. Mechanical behaviors such as stress and strain dictate the occurrence of cracks and loss of contact, and are intimately related with the morphology and mechanical properties of electrode active and inactive materials. During charge and discharge, the amount of Li in the electrodes varies, causing the host electrodes to experience phase transformation and volumetric change [23]. The deformation can be constrained by various conditions such as grain boundaries, mismatch between active and inactive materials, and inhomogeneous distribution of Li ions. Such constrained conditions generate a stress field that induces fracture and morphological change.

Figure 1.3 summarizes different forms of mechanical degradation observed in LIBs materials which are detrimental to the electrochemical performance of batteries.

In most cases, electrode deterioration ultimately causes detachment of active material from electrode, leading to irreversible capacity loss and impedance rise. One common form of degradation is the occurrence of cracks that form to relieve stresses induced by the volumetric mismatch between lithiated and delithiated phases. Wang et al. [24] found evidence that, during lithiation, $LiFePO_4$ grains turns into a two phase structure of $LiFePO_4$ and $FePO_4$ with a sharp interface. When this interface is subjected to stress resulted from volumetric change, cracks form and grow as shown in Figure 1.3a. Crack

formation related with two phase boundary is also observed in silicon nanoparticles in the work of Liu el al. [25]. The mechanism of lithiation in crystalline Si particles can be described as an inward movement of the two-phase boundary between the inner core of pristine Si and the outer shell of amorphous Li–Si alloy. In this case, the crack is initiated at the outer shell by buildup of large tensile hoop stress (Figure 1.3e).

Delamination between active particles and binders is another common manifestation of degradation in LIB. During delithiation, the active particles shrink and, because of the inherent plasticity of binders, the matrix do not restore fully to its initial configuration, leaving a gap between active material and matrix [26]. This mechanism was observed by Chen [27] in $LiMn_{1.95}Al_{0.05}O_4$ (LMAO) electrodes after being subjected to 1015 cycles (Figure 1.3c).

Evidence of particle disintegration has been observed in electrode materials where active particles are formed by an agglomerate of smaller particles, defined as primary particles. This type of degradation has been studied by Watanabe et al. [28] for $LiAl_{0.10}Ni_{0.76}Co_{0.14}O_2$ (NCA) electrodes and shown to be closely related to the depth-of-discharge (Figure 1.3b). At tests performed with wider discharge windows, the volumetric expansion is more expressive, thus introducing higher stresses in the material. This leads to the generation of micro-cracks that are responsible for the separation of primary particles.

Material pulverization is a degradation mechanism observed in electrodes that experience high volumetric expansion due to insertion and extraction of a large amount of lithium. The experiment conducted by Liu et al. [29] on aluminum nanowire found evidence of this effect. The dealloying of lithium from LiAl eventually gives rise to

pulverization of the metallic nanowire electrode forming Al nanoparticles separated by voids (Figure 1.3f).

There are also cases where the volumetric expansion leads to SEI breakage. Sun et al. [30] found the evidence of this effect in Co_3O_4 hollow spheres after 90 cycles at 1C, shown in Figure 1.3d. This degradation of the SEI is detrimental to electrochemical performance of the battery because when the SEI fractures, new surfaces of the active material are exposed to electrolyte, inducing the formation of new SEI. This process keeps decomposing the electrolyte and consuming lithium ions and results in a persistent decrease of cyclic efficiency.

Failure mode	Examples
(a) Cracks in cathode particle due two phase boundary	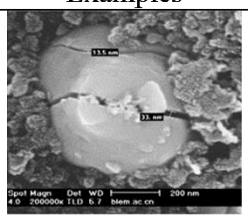 LiFePO4 particle after 60 cycles
(b) Primary particle disintegration	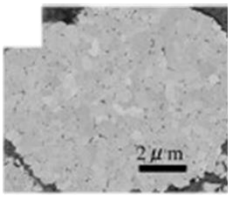 Pristine NCA 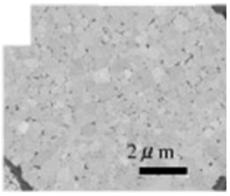 10–70% DOD, 25 °C 2500 cycles 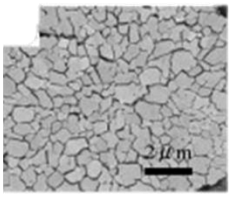 0–100% DOD, 60 °C 350 cycles
(c) Debonding between particle and matrix	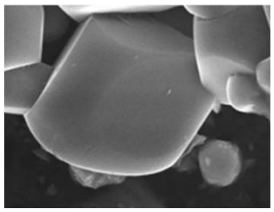 Pristine LMAO 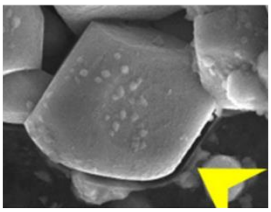 Cycled LMAO
(d) SEI breakage	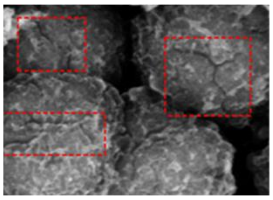 Cycled hollow Co_3O_4 spheres
(e) Crack in anode nanoparticle due two phase boundary	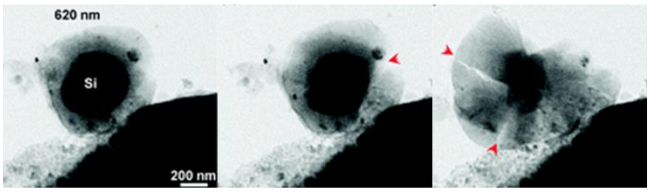 Partially lithiated Si Crack initiation Crack growth
(f) Voids by pulverization	Pristine aluminum  After 4 cycle 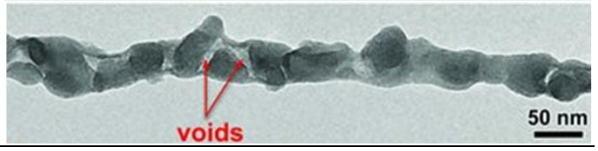

Figure 1.3. Common mechanical degradation in LIBs [24] [25] [27] [28] [29] [30].

1.3 Mechanical characterization of electrodes

Section 1.2.1 demonstrated how structural changes and degradation affect the electrochemical performance of LIBs. This chapter presents an overview of different techniques that can be applied for the evaluation of mechanical stabilities of electrodes, and provides arguments that support the experimental method developed in this work.

Mechanical characterization techniques consist of standardized measurements of how materials respond to physical forces. Mechanical properties acquired through these tests are essential for modeling mechanics of electrodes and predicting cycle life. Thus, they can help advance the current understanding of how mechanical degradation is induced, and clarify the relationship between mechanical properties and capacity fade. This information assists the fine tuning of electrode composition and microstructure, to minimize degradation and improve capacity retention. The following subsections describe the most commonly used mechanical characterization techniques in the field of energy storage materials.

1.3.1 Wafer curvature method

Curvature-based experimental techniques are used to monitor stress evolution and measure the biaxial modulus of thin films. The stress is induced during thin film deposition and by other processes such as, in the case of in-situ measurements of lithium ion batteries, the volume expansion due to lithiation. The stress cannot be directly measured since it is a field variable, however, it can be estimated through the measurement of deformation [31]. Stress in a thin film on a flexible substrate induces a curvature of the substrate, as illustrated in Figure 1.4. This change in curvature is used to calculate the stress through the Stoney's

equation [32], which is also a function of the biaxial modulus of the substrate, and the thickness of both the film and the substrate.

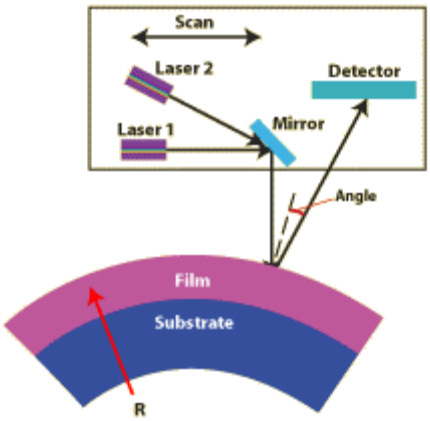

Figure 1.4. Schematic of wafer curvature methods [31].

This method has been successfully applied to measure in-situ stress evolution in materials in Li-ion cells [33] [34]. The biaxial modulus can be estimated by performing a sequence of lithiation/relaxation/delithiation steps at several values of state-of-charge (SOC). The biaxial modulus is given by the stress change estimated from the curvature test ($\Delta\sigma$) and volumetric strain of the film due to lithiation ($\Delta\varepsilon$), which is proportional to the amount of lithium inserted [35].

1.3.2 Tension and compression tests of battery packs at large scale

Tension and compression tests probe fundamental material properties such as elastic modulus, yield strength, and ultimate strength through the analysis of stress-strain curves [36]. In general, these tests are conducted by fixing the specimen into a test apparatus and applying a force to the specimen by separating or moving together the testing

machine crossheads. Macro mechanical tests have limited application in LIB characterization due to the small characteristic size and heterogeneous structure of electrode components. Therefore, in LIB research, this technique is most commonly used to evaluate mechanical integrity of systems and major components, instead of the intrinsic properties of constituent materials. For example, Peabody and Arnold [37] have employed tension and compression tests to evaluate the rate and fluid-dependent mechanical properties of separators immersed in different fluids, as illustrated in Figure 1.5. This type of test can also be coupled with electrochemical analysis to study short circuiting behaviors of battery packs at different SOC [38].

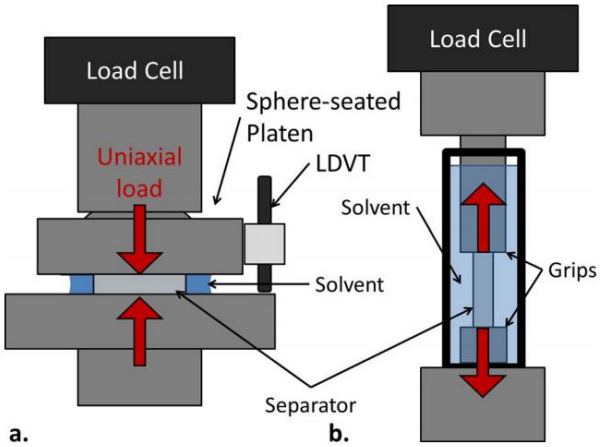

Figure 1.5 Schematic of (a) compression and (b) tension tests of samples immersed in fluid [37].

1.3.3 Tensile test of single nanowires and nanotubes at nanoscale

In the recent years, the interest in nanowire and nanotube structures for high capacity electrodes has motivated the development of different techniques to perform mechanical testing on 1-D nanostructures. In general, these experiments require at least one high resolution actuator coupled with one high precision microscopy system to monitor

deformation. One example is the device developed by Lu et al. [39] shown in Figure 1.6, which is able to convert the compressive force applied by a nanoindenter into pure tension loading at the sample stage where a nanowire is fixed. The in-situ characterization in Li-ion batteries adds more complexity to the experiment. The system designed by Kushima et al. [40] can conduct lithiation of silicon nanowires followed by tensile test of the lithiated nanowire. A 3D piezoelectric manipulator is responsible for applying tension load to the wire, while the deformation is measured from the TEM images. In addition, an AFM cantilever is employed to exchange modes from electrode charging to mechanical testing and vice-versa. Figure 1.7 summarizes the test procedure.

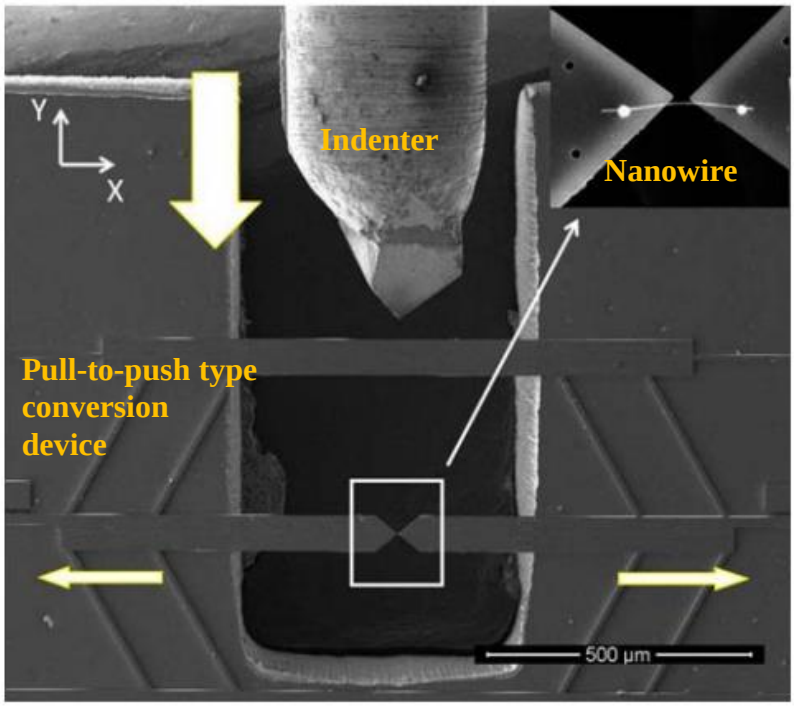

Figure 1.6. Device by Lu et al. [39] that allows carrying out tensile testing using instrumented indentation and TEM imaging. Arrows show the direction of movement; the load is applied on the device downwards and converted into axial tensile loading at the nanowire.

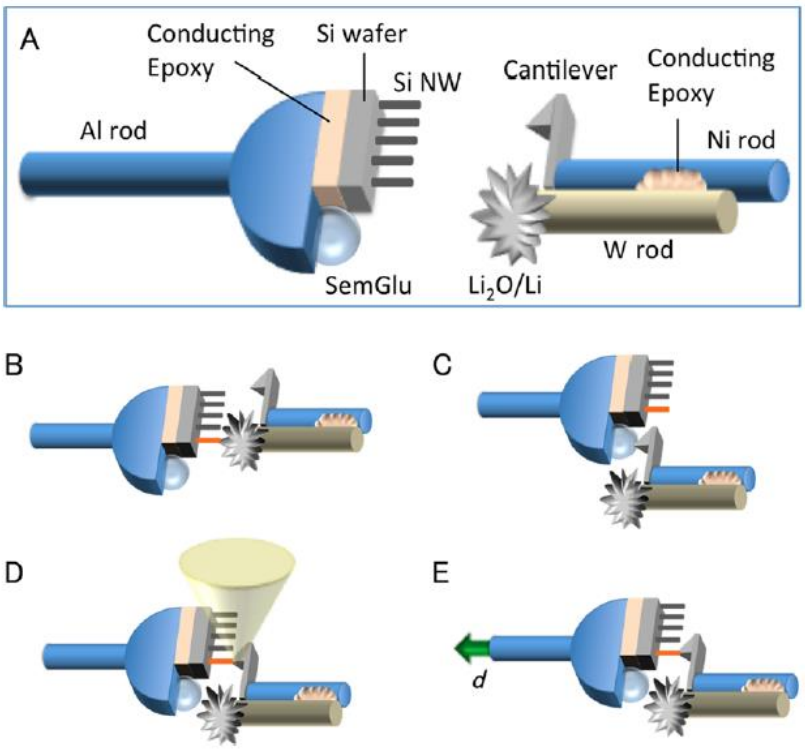

Figure 1.7. In situ TEM tensile experimental procedure by Kushima et al. [40]. (a) Illustration of main components. (b) Silicon nanowire is first lithiated using lithium metal as the counter electrode (c) An AFM controls the cantilever to contact with a glue. (d) The cantilever is moved to touch with the tip of the nanowire. (e) Tensile test is carried on by a displacement controlled piezo movement.

1.3.4 Nanoindentation

Instrumented indentation is a well-established technique that can be applied in the characterization of a variety of materials and structures including biological specimens, thin films, metals, polymers and composites. It is capable of testing a range of mechanisms such as dislocation, fracture, creep, fatigue, scratch resistance, and so on [41] [42] [43]. The most common mechanical properties assessed by nanoindentation tests are elastic modulus and hardness.

The test procedure starts with a hard tip applying pressure to the sample and, as the load increases, the tip penetrates into the specimen (Figure 1.8). Elastic and plastic deformation yield an impression conforming to the shape of the tip, until it reaches a user-defined load or displacement value. When the load is removed, the elastic portion of the deformation is recovered, leaving a residual indentation on the sample. Force and tip displacement are continuously controlled and measured with high resolution actuators and sensors throughout the loading cycle and the contact area is inferred from the resulting load-displacement curve data, discarding the need for imaging the residual impression. Finally, the mechanical properties are derived from the load-displacement data. The theory behind the estimation of the mechanical properties is explained in detail in Section 2.1.

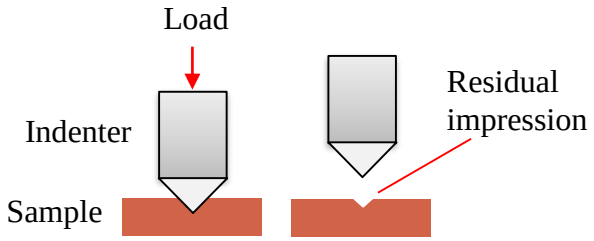

Figure 1.8. Schematics of indenter penetration and residual impression

The instrumented indentation technique has been widely employed in the characterization of energy storage materials for enabling the investigation a range of deformation mechanisms and materials, and more specifically, being suitable to materials of small characteristic size such as of micrometer size particles, thin films and even the SEI layer, in the case of nanoindentation using atomic-force microscopy (AFM) [44].

1.4 Thesis outline

The goal of this thesis is to develop high-throughput and in-situ experimental techniques for mechanical characterization of electrode materials that will assist in advancing the current understanding of the relationship between mechanical stability and electrochemical performance of LIBs. The thesis structure is organized as follows. Section 2 describes in detail the mechanical characterization device used in this work and the theory supporting the derivation of mechanical properties. Section 3 introduces a method for the characterization of composite materials, so-called grid indentation. This method is applied to a state-of-art cathode material and the results are validated against tests performed on bulk materials. Finally, Section 4 presents a novel experimental platform for in-situ mechanical characterization of Li-ion electrodes during lithiation. This technique is applied for silicon electrodes and is validated against literature data.

2. INSTRUMENTED INDENTATION

The most common mechanical properties measured through nanoindentation are the hardness and elastic modulus. The elastic modulus is an intrinsic material property fundamentally related to atomic bonding. Hardness, however, is a specific engineering measurement of a material's resistance to localized deformation, and it gives an indication of the strength of the indented material. In general, a simple relationship between hardness H and yield strength Y for metals is given by [45]:

$$H \sim 3Y. \tag{2.1}$$

The Keysight G200 nanoindenter is employed in this work. The head assembly of this system is illustrated in Figure 2.1. In order to apply load to the sample, a magnetic field is first generated by a varying electric current on the coil. This controlled magnetic field interacts with the magnetic field of a permanent magnet, moving the indenter column up and down. The displacement is continuously measured by a capacitive gauge. Ultimately, each indentation generates a load-displacement curve that is used to calculate the mechanical properties of the specimen.

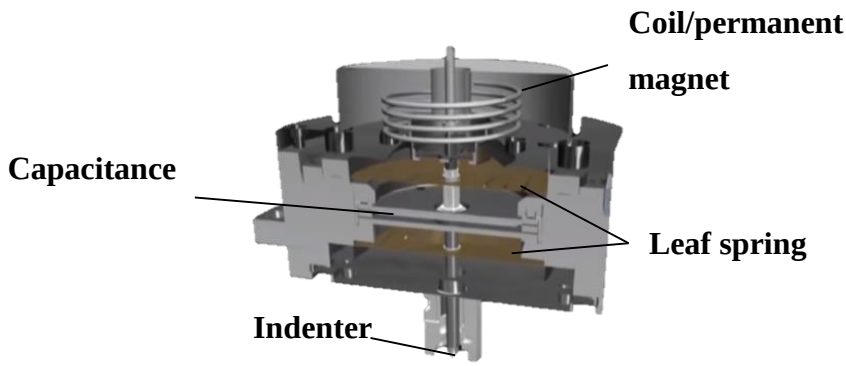

Figure 2.1. Keysight XP nano-mechanical actuator and transducer.

Different tip geometries and sizes can be employed depending on the application. The most common indenter geometries are illustrated in Figure 2.2, along with a list of recommended applications by Keysight [46]. The Berkovich tip is ideal for most applications. It can generate reliable data for most materials and it is suitable for indentation tests ranging from nano- to microscale.

Berkovich	Vickers	Cone	Sphere
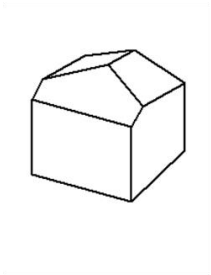	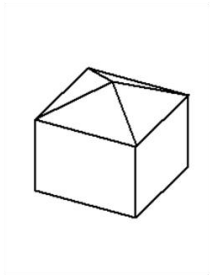	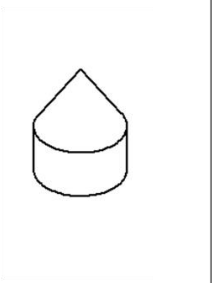	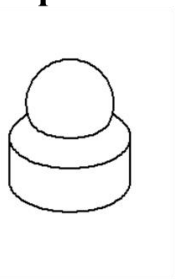
• Bulk Materials • Thin Films • Polymers • Scratch Testing • Wear Testing • MEMS • In-situ Imaging	• Bulk Materials • Films and Foils • Scratch Testing • Wear Testing	• Scratch Testing • Wear Testing • In-situ Imaging • MEMS	• MEMS

Figure 2.2. Most common tip geometries and corresponding applications.

2.1 Theory

This section covers the derivation of the elastic modulus and hardness from the load-displacement curve. An example of a typical load-displacement curve along with the main parameters used in the following calculations are presented in Figure 2.3a

The hardness is defined as the maximum applied load P_{max} divided by the corresponding contact area A.

$$H = \frac{P_{max}}{A(h_c)}. \tag{2.2}$$

While P_{max} is directly measured from the load-displacement curve (Figure 2.3a), the contact area A is calibrated empirically as a function of the contact depth h_c. The calibration of the area function is covered in the Section 2.2.

The estimation of h_c is based on the assumption that contact periphery of the indented area behaves as a rigid punch on a flat elastic half-space, sinking in during penetration, as illustrated in Figure 2.3b [47]. Thus, the contact depth is given by the displacement at maximum load h_{max} and the total amount of sink-in $h_s = \epsilon P_{max}/S$, where ϵ is a constant that depends on the tip geometry - ϵ=0.75 for the Berkovich tip - and S is the slope of the unloading curve during indenter removal.

$$h_c = h_{max} - h_s \tag{2.3}$$

Notice that not all materials behave this way. For ductile materials, instead of sinking down, the surface around the indenter sometimes is squeezed out upwards around the indenters. This effect is discussed in detail in Section 2.3.3.

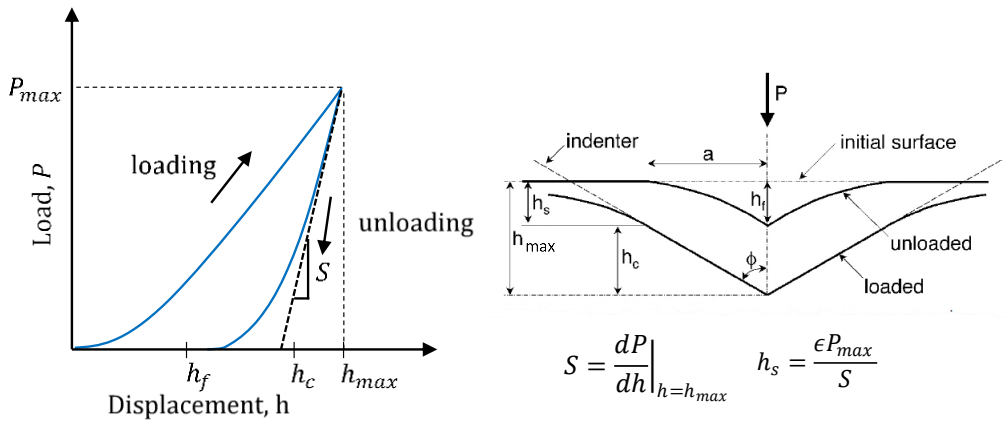

Figure 2.3. (a) Schematic of the load-displacement curve. (b) Contact geometry parameters [47].

In order to calculate the contact stiffness S, the upper portion of the unloading curve is first fitted by the power-law relationship proposed by [47],

$$P_{fit} = B\left(h - h_f\right)^m, \tag{2.4}$$

followed by analytical derivation of P_{fit} at the maximum load,

$$S = \frac{dP_{fit}}{dh}\Big|_{h=h_{max}} = mB\left(h_{max} - h_f\right)^{m-1}. \tag{2.5}$$

Finally, the elastic modulus E is given by the contact mechanics expression for the reduced modulus E_r, which takes into account the deformation of both indenter and sample.

$$\frac{1}{E_r} = \frac{1 - v^2}{E} + \frac{(1 - v_i^2)}{E_i}. \tag{2.6}$$

While the properties of the indenter (v_i,E_i), and the Poisson ratio v of the sample are known, E_r is derived from the test data as follows

$$E_r = \frac{S\sqrt{\pi}}{2\beta\sqrt{A}}, \tag{2.7}$$

where β is a known dimensionless constant that depends on the geometry of the indenter tip.

2.2 Area function calibration

The area function defines the relationship between the cross-sectional area of the indenter to a distance of its tip. This function is calibrated empirically to account for non-idealities on shape of the indenter. The mathematical form presented below is used in the calibration for its ability to fit data over a wide range of indentation depths and a number of indenter geometries [47].

$$A(h_c) = C_0 h_c^2 + \sum_{i=0}^{n} C_i h_c^{\frac{1}{2^i}}. \tag{2.8}$$

The coefficients C and number of terms n are selected to best fit the experimental data of a standard material of known properties. For this work, the calibration is performed on fused silica. The area function is fitted for a range of indentation depths as shown in Figure 2.4, where each point corresponds to one indentation. The data shows an average elastic modulus and hardness approximately constant over the depth range of 50 nm to 1900 nm, that match standard values for fused silica of 72.5 GPa and 9.95 GPa, respectively [48]. The data scatter increases significantly for tests performed below 100 nm depth. Even though data is more scattered at shallower indentations, 16 tests performed at 100nm still display a reasonable estimate of the both modulus and hardness of 73.5 GP and 9.15 GPa, respectively.

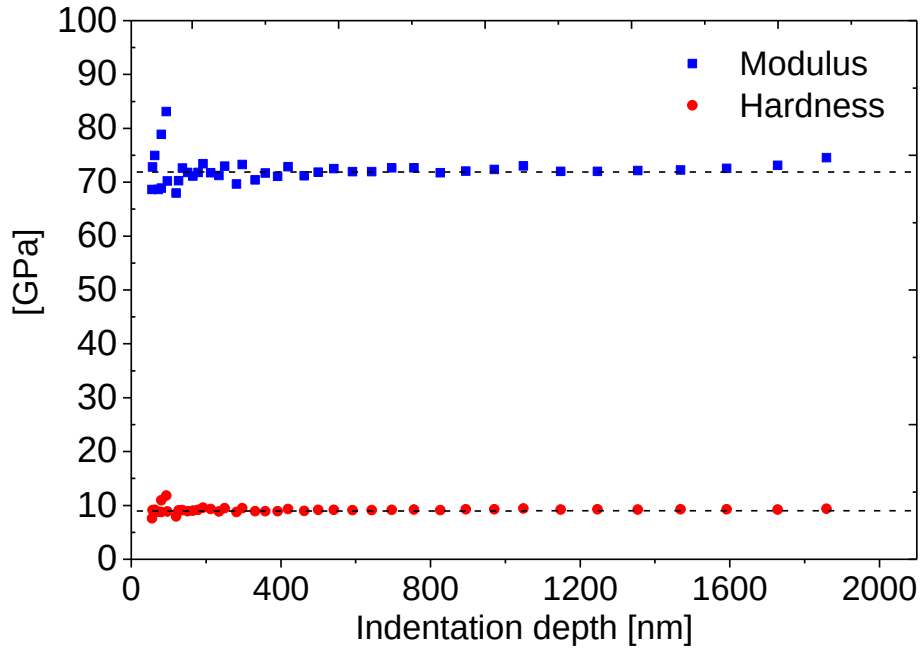

Figure 2.4. Area function calibration test on fused silica.

2.3 Sources of error

2.3.1 Creep

It is important to analyze the shape of load-displacement curves in order to verify the deformation mechanisms. During unload, a viscoelastic material may display additional penetration due to the continued creep, leading to a bowing out effect in the load-displacement curve as shown in Figure 2.5 by Bushby et. al [49]. This behavior leads to an overestimation of the elastic modulus, since it translates into an increased value of the stiffness constant S. To prevent time-dependent behavior from interfering with calculations, the material can be allowed time to creep prior to unload, by holding the peak load constant for a sufficient period of time. The creep rate decreases with the hold time. According to the International Organization for Standardization (ISO) 14577, the creep rate at the end of

the hold period should be less the 1/10th the unloading rate. In order to determine if the creep displacement is saturated during the peak hold, different hold times can be tested and compared to confirm the same material response [50].

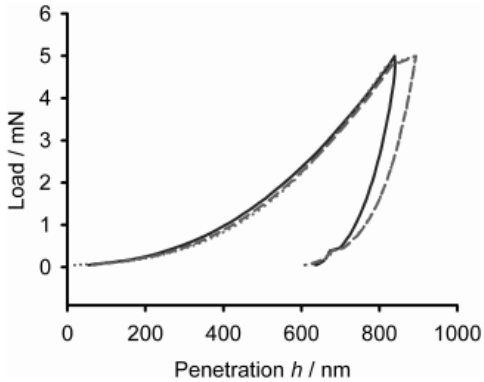

Figure 2.5. Solid line (no peak hold time) shows elbow in the unloading curve due to continued creep. Dashed lines (120s and 240s peak hold time) with creep saturated during the peak hold time [49].

2.3.2 Thermal drift

Another factor that can contribute to the variation of the penetration depth during constant load is the drift due to thermal expansion. The drift can be minimized by placing the equipment inside an enclosure that blocks air flow, however, it cannot completely prevent it. Thus, it is necessary to perform a correction in the test data in order to account for this effect. The drift correction procedure is explained in Figure 2.6 by Wheeler et al. [51], which shows the tip displacement as a function of time. During unload, the load is held constant at 10% of the peak load (solid line) for several seconds. The rate of change of the indentation depth during the hold time is recorded (red dashed line), and the slope is calculated and assumed to be constant throughout the entire test (green dashed line). The

raw displacement data (red dashed line) is then corrected with the calculated drift (blue dashed line). The corresponding load-displacement curves before and after the drift correction are shown in the inset figure.

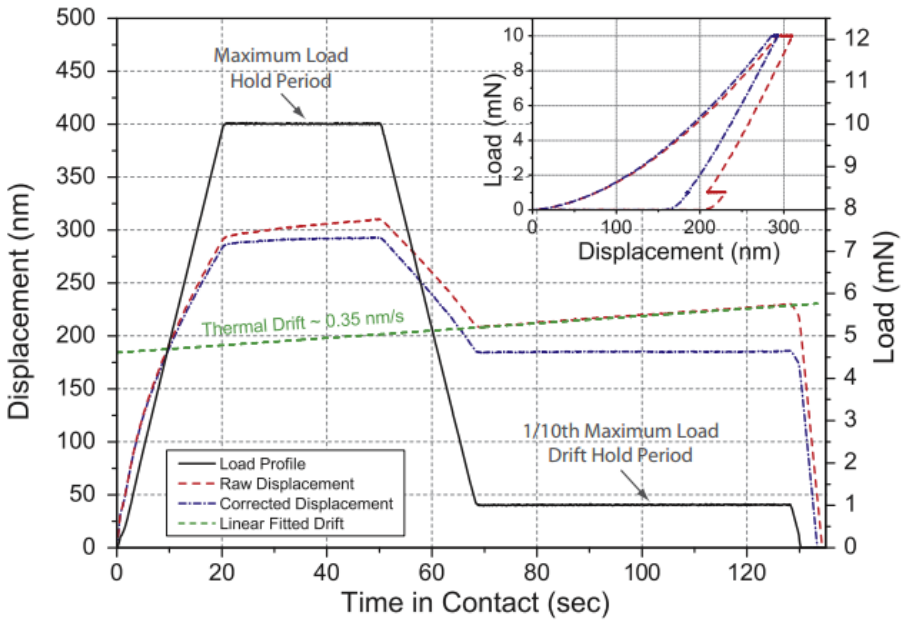

Figure 2.6. Standard thermal drift correction procedure [51].

2.3.3 Pile-up

As described in Section 2.1 and Section 2.2, in instrumented indentation (depth-sensing indentation), the contact depth h_c and contact area A are estimated from the load displacement curve via Equation (2.3) and Equation (2.8). In this approach, it is assumed that the surface around the indenter sinks down during test. However, there are cases where the periphery of the surface may pile up instead of sinking down. In those cases, if no correction for pile-up is performed, the contact area is underestimated and, consequently, the mechanical properties are overestimated.

Oliver et al. [47] found a simple quantity that can be used to assess whether or not a material is likely to pile-up. This parameter is the ratio between the final depth of the imprint after unloading h_f and the maximum indentation depth h_{max}, which can be easily extracted from the load-displacement curve. Pile-up is large only when h_f/h_{max} is close to 1 and the material is not expected to work harden during the indentation. For $h_f/h_{max}<$ 0.7, very little pile-up or no pile-up is expected independently of the material work-hardening behavior.

2.3.4 Substrate effect

Nanoindentation requires the user to specify either the maximum penetration depth, or the maximum load for a given test. These two parameters are especially important for the evaluation of structures of small characteristic size. For example, if the sample is a thin film, it is imperative that the user selects a maximum indentation depth that is sufficiently shallow to produce substrate independent measurements. In general, the maximum penetration depth should be less than 10-25% the thin film thickness to avoid substrate effects [52] [53] [54].

2.3.5 Surface roughness

The derivation of the mechanical properties from indentation test data is based on the assumption of a flat surface and, therefore, the quality of a sample surface can interfere with measurements. In a non-uniform contact, the indenter can either come into contact with a peak or valley. Contact with a peak intensifies localized stress, leading to a larger depth of penetration at a given load, consequently underestimating the hardness. The

contact with a valley leads to a higher contact area, smaller material deformation and as a result, an overestimation of the mechanical properties [55]. The International Standard ISO 14577-4 recommends that the surface roughness should be less than 5% the maximum penetration depth. However, studies have reported that repeatable and accurate measurements can be obtained for samples exhibiting roughness values significantly higher than 5% of the maximum indentation depth, as long as a sufficient number of indentations are performed [56].

3. GRID INDENTATION OF COMPOSITE ELECTRODES

3.1 Introduction

Electrodes in commercial batteries are materials of high heterogeneity at the nano- to microscale consisting of metal- or ceramic-like active materials, polymeric binders, and porous carbon black conductive matrix. The constituents have a large difference in their mechanical properties – the elastic modulus changes by 2-3 orders of magnitude for instance. Determining the mechanical properties of individual phases in heterogeneous structures is a challenge.

A common approach to obtain the properties of individual phases in a heterogeneous material is performing selective indentation at the desired phase only. This process requires careful selection of the indentation location and examination to ensure that results are not affected by the surrounding medium [57]. A faster and more practical alternative is to use the grid indentation technique followed by statistical deconvolution [58] [59].

Grid indentation relies on a massive array of nanoindentation and statistical deconvolution of experimental data to extract the mechanical properties of individual components. An illustration of a material composed of two phases of distinct properties is shown in Figure 3.1a. Each triangle in the image corresponds to the imprint of one indentation test. Provided that the indentation depth is much smaller than the characteristic size of the two phases and the grid spacing is larger than the size of the indentation

impression, a large number of indentations on the sample surface probe the mechanical properties of either phase with the probability that equals the surface fraction. Assuming that the distribution of the mechanical property of each phase can be described by a Gaussian distribution [60], grid indentation yields a multimodal probability function that allows determination of properties of each phase, Figure 3.1b.

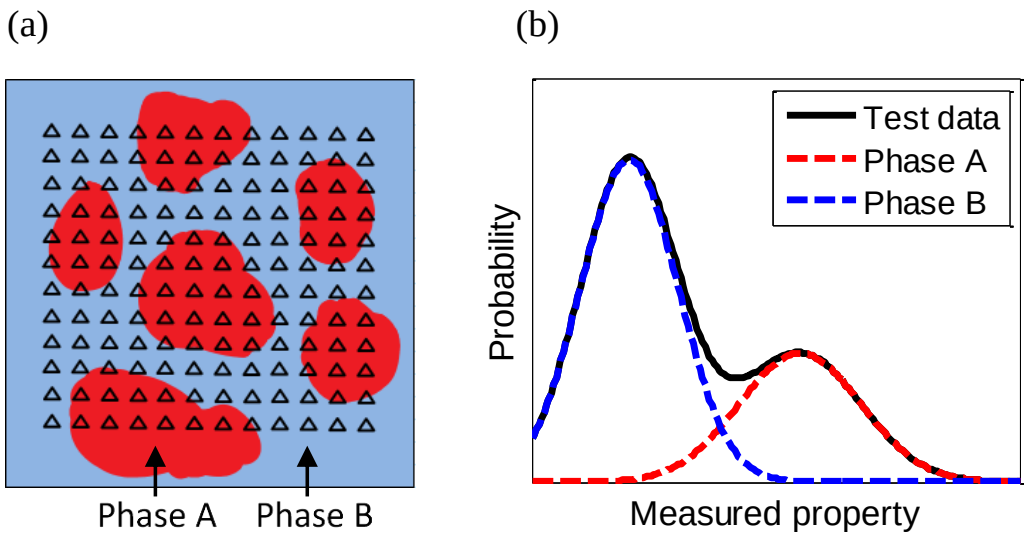

Figure 3.1.(a) Schematic of grid indentation on a heterogeneous material. The red and blue colors represent different phases, and the triangles represent individual indentation sites. The indentation size is much smaller than the characteristic size of the phases and the grid spacing is larger than the size of indentation impression. (b) Grid indentation yields a multimodal probability function that allows determination of mechanical properties of the constituent phases.

The grid indentation method was explored by Constantinides et al. [60] for the model composite of titanium-titanium monoboride which set up guidelines for the application of this technique. Ulm et al. [61] employed the grid indentation technique to separate the intrinsic and the structural sources of anisotropy of hydrated particles in concrete, bone and shale at different length scales. Furthermore, the authors advance the traditional statistical

analysis procedure to enable accessing packing density distributions in the addition to the mechanical properties.

In the context of composite electrodes, the grid indentation method was far less exploited. The main challenge in employing this technique in the evaluation of electrode materials lies on the substantial difference in the mechanical properties of its constituents. The combination of material phases of irregular shape, small characteristic size, and vastly distinct properties makes it difficult to extract the properties of single constituents without being affected by the surrounding medium.

Amanieu et al. [62] employs selective indentation followed by statistical deconvolution to extract the properties of a $LiMn_2O_4$ cathode. The technique includes performing grid indentation over the surface of the composite and then discarding indentation tests that displayed mixed phase properties by identifying, through a novel method, the composite behavior in the load-displacement curves. The method showed to be more efficient to filter the single phase properties of a reference sample made of silica and epoxy than for the commercial battery electrode due to the higher complexity of its microstructure. The authors opt for embedding the sample in epoxy for mechanical stability during polishing and indenting, therefore altering the properties of the porous matrix.

In this work, it is shown that an appropriate selection of the indentation depth, careful sample preparation for high quality surface finish and application of a robust optimization algorithm, makes it is possible to obtain reliable single phase properties from grid indentation tests on composite electrodes. The grid indentation method is applied to a model system of $LiNi_{0.5}Mn_{0.3}Co_{0.2}O_2$ (NMC 532) cathode for commercial batteries and results are validated with selective indentation at individual material phases. The analysis

provides valuable insights on the advantages and limitations of the grid indentation method in the evaluation of composite electrodes.

3.2 Overview of NMC cathode

Since its introduction in 1980, oxides compounds based on transition-metal elements have been used as cathode materials in LIBs and its composition widely studied for improved performance, safety and cost [63]. $LiNi_xMn_yCo_{1-x-y}O_2$ (NMC) is a class of cathode material attractive for the electric vehicle applications, that is gradually replacing $LiCoO_2$ in consumer batteries [64] [65]. NMC is comprised of alternating Li and transition-metal layers where the composition of Ni, Mn, and Co and morphology can be tuned to optimize performance in terms of capacity, cyclic rate, electrochemical stability, and lifetime. Ni provides a higher specific energy while Mn improves thermal stability [66]. Furthermore, compounds containing large amounts of Ni, such as in $LiNi_{1-x}Mn_xO_2$, are known to display low Li diffusivity, resulting in a low-rate cathode material. Adding Co has proved to be effective to address this issue [65]. The NMC 532 has a well-balanced ratio of Ni, Mn and Co that offers reasonably good thermal stability, high capacity, and due to its lower content of Co compared to the $LiCoO_2$ cathode, it allows for low and stable pricing, while still maintaining the higher rate capability [63][66]. The NMC is current a state-of-art material for LIBs, however, its mechanical properties have been widely unknown [67] [68].

3.3 Material preparation and experimental details

3.3.1 Electrode processing

As-received $LiNi_{0.5}Mn_{0.3}Co_{0.2}O_2$ (NMC532, Toda America) powders, polyvinylidene fluoride, (PVDF, Solvay, 5130), carbon black (CB, Denka, powder grade), and N-methylpyrrolidone (NMP, Sigma Aldrich) were used to prepare the NMC cathodes by slot-die coating. Sample composition consists of 90 wt% NMC532, 5 wt% PVDF, and 5 wt% CB. Detailed fabrication method can be found in reference [69]. The areal loading of the NMC cathode is 12.5 mg/cm^2 and as-prepared samples were not calendered.

3.3.2 Microstructure characteristics

The scanning electron microscopy (SEM) images of the NMC cathode is presented in Figure 3.2. The electrode microstructure consists of nearly spherical NMC particles and a porous matrix composed of a mixture of CB nanoparticles and PVDF binder. A magnified view on a single NMC532 particle closely packed by primary particles is shown in Figure 3.2b. The particle size distribution obtained from approximate measurements on a representative surface area of the electrode showed a significant variability in particle size, ranging from approximately 2µm up to 14 µm. The electrode thickness (excluding the Al current collector) ranges from 45 to 57 µm as shown in Figure 3.2c.

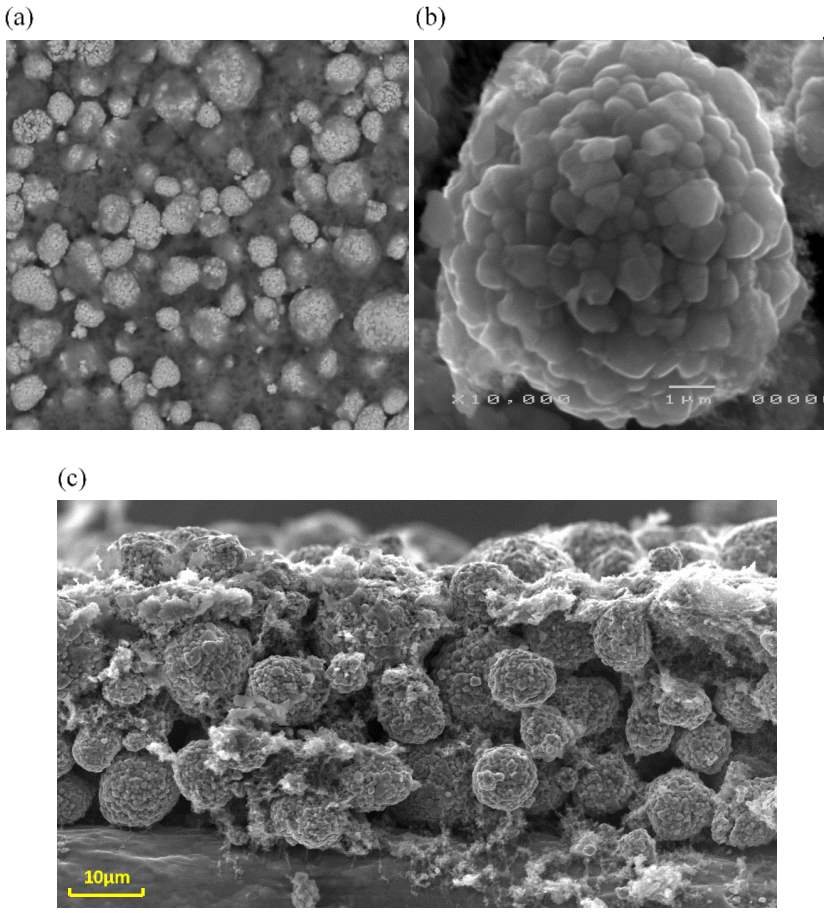

Figure 3.2. SEM images of the cathode electrode composed of NMC532 particles, PVDF binders, and porous carbon black matrix. (a) Top view. (b) Magnified view on a single NMC532 particle. (c) Cross-section view.

3.3.3 Surface preparation

The highly irregular surface of the sample required polishing in order to obtain a smooth and flat surface suitable for indention tests. Polishing is challenging for porous composites made of soft and hard phases; particle removal and material delamination from aluminum foil are common problems. The following procedure showed the best results for the NMC cathode. First, the samples are adhered to a glass slide using Crystalbond. The polishing process starts with coarse polishing using a two-step diamond polishing. In the

first step, a 3 µm diamond paste is applied along with a microid diamond extender on Ultrasilk cloth mounted to a polishing wheel and the sample is polished for approximately 1 to 3 minutes. The sample is then washed and, in the second polishing step, a 1 µm diamond paste on Red felt cloth is used, applying the same polishing procedure. Most of the particle surface is exposed during this coarse polishing as shown in Figure 3.3b. In the final polishing step, 0.05 µm colloidal silica is applied on Imperial cloth and the sample is polished from 2 to 5 hours on moderate pressure using an automatic head (Buehler AutoMet 2000). The quality of the surface is evaluated on an optical microscope every 30 minutes. Once the surface is free of scratches and dark spots (Figure 3.3c), the sample is rinsed and dried for mechanical measurements. As expected, the drying procedure did not affect mechanical measurements; samples vacuum dried overnight at 90 °C or dried manually with a wipe exhibited same mechanical properties. A SEM image of the sample surface after final polishing is shown in Figure 3.4.

Figure 3.3. Surface preparation procedure. Optical images of the NMC surface (a) as-coated, (b) after coarse polishing and (c) after fine polishing.

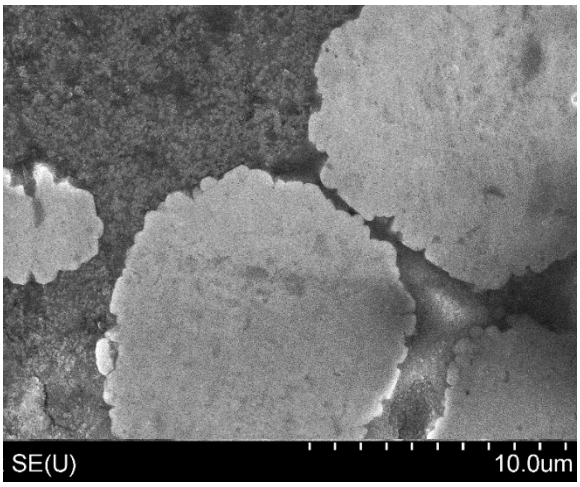

Figure 3.4. Close-up view of the polished surface of the NMC electrode.

3.3.4 Indentation test setup

The Keysight G200 nanoindenter was employed to measure the mechanical properties of the electrode. Indentation tests were performed using Berkovich tip and at a constant strain rate of 0.05 s^{-1}. Poisson ratio of 0.3 and 5 s peak hold time were used.

Grid indentation technique is suited for composite electrodes as long as the indentation depth is sufficiently small to probe the mechanical properties of an individual material phase. The shallowest indentation depth allowed by our test equipment for high precision measurements on a smooth surface is approximately 100 nm, as demonstrated in Section 2.2. Experimental and modeling studies on thin films showed that a maximum penetration depth of less than 10% the thickness of the thin film is generally sufficient to avoid substrate effects, as discussed in Section 2.3.4. An analogy can be made of indentations performed on composites to indentations performed on thin films [60]. Thus, the characteristic sizes of a given material phase in the composite can be used to evaluate whether or not measurements at a given indentation depth are likely to be significantly affected by the surroundings. As verified by the SEM images presented in Section 3.3.2,

the particle size of NMC particles vary from 2 µm to 14 µm. Thus, one can expect that the indentation depth of 100 nm will be sufficiently shallow to measure the mechanical properties of NMC, without significant interference of the matrix properties. The nanometer characteristic size of the CB agglomerates mixed in the PVDF binder makes individual measurements unfeasible. Thus, the CB and PVDF mixture is regarded as a single phase referred as CB/PVDF phase. Still, it is difficult to predict the accuracy in which the grid indentation method is able capture the matrix properties due to its irregular shape and non-uniform size; thus this metric can only be investigated through experimental validation, as presented later in Section 3.6.

The spacing between the indents is set to 3-5 µm, which is more than 20 times the maximum indentation depth, as recommended by the manufacturer in order to avoid interference between indentations [48].

3.4 Statistical analysis

Given that the constituents possess distinct mechanical properties; grid indentation yields a multimodal probability function that allows determination of each phase using statistical analysis. An optimization algorithm can be used to fit a function the test data and extract the properties of each material phase.

In order to select the function that can be used to describe the distribution of mechanical measurements in a homogeneous material, consider the two sources of variability in results: errors in experimental measurements and inhomogeneity in the material properties.

In experimental measurements, systematic errors can appear as a result of bad calibration or inappropriate experiment setup; significant systematic errors can be ruled-out in our experiment given that all necessary measures of precaution are satisfied regarding equipment calibration (Section 2.2) and requirements to avoid different sources of errors (Section 2.3). Random errors are product of aleatory events, such as electronic noise in signal processing or random changes in environmental conditions. These errors are expected – it can be clearly seen from the area function calibration that random noises arise at shallower indentations due to the increased sensitivity to the surface roughness and limitations in the equipment displacement and load resolution.

Considering the material properties, in this case either CB/PVDF or NMC particles, the possible sources of variability in its mechanical properties are also expected to be random. In the NMC particle, it can be due to tests performed in randomly orientated crystals, while in the matrix it can be due to variations in the concentrations of CB and PVDF. Since the only substantial sources of variation in the measured properties are expected to be random, for the sake of simplicity, it is satisfactory to assume that the mechanical property distribution is approximately Gaussian.

Let x be the measured mechanical property – in this case, it is either elastic modulus E or hardness H. Assuming that the mechanical property of each phase obey a Gaussian distribution function, the theoretical cumulative distribution function C_i (CDF) of the *i-th* phase is given by

$$C_i(x) = \int_0^x \frac{1}{\sigma_i\sqrt{2\pi}} e^{-\frac{(u-\mu_i)^2}{2\sigma_i^2}} du \quad , \tag{4.1}$$

where μ_i is the mean value and σ_i the standard deviation.

Let f_i be the normalized surface fraction of the *i-th* phase with the condition $\sum_{i=1}^{n} f_i = 1$, n the total number of phases and C_{exp} the normalized cumulative distribution of the experimental data. The unknowns $\{f_i, \mu_i^E, \sigma_i^E, \mu_i^H, \sigma_i^H\}$ are determined by minimizing the difference between the experimental CDFs and the weighted modal-phase CDFs while maintaining the same surface fraction f_i in the elastic modulus and hardness CDFs,

$$\min\left[\left(\sum_{i=1}^{n} f_i C_i^E - C_{exp}^E\right)^2 + \left(\sum_{i=1}^{n} f_i C_i^H - C_{exp}^H\right)^2\right]. \tag{4.2}$$

Here C_{exp}^E and C_{exp}^H correspond to the experimental cumulative distributions for elastic modulus and hardness, respectively. The results of statistical deconvolution are estimates of the mean and standard deviation of elastic modulus and hardness of each phase, and surface fraction.

The fitting is additionally constrained by a moving boundary set at one standard deviation distance from the mean value of each modal-phase, according to

$$\mu_i + \sigma_i < \mu_{i+1} - \sigma_{i+1}\,, \tag{4.3}$$

where $\mu_i < \mu_{i+1}$. This constraint is set to prevent excessive overlapping between Gaussian distributions.

The curve fitting is performed using the open source Matlab based genetic optimization toolbox GOSET 2.6 available at [70]. The algorithm requires minimum input from the user and is able to consistently converge to the global minimum as opposed to local minimums. The optimization algorithm is set to generate 3000 different combinations of individuals $\{f_i, \mu_i^E, \sigma_i^E, \mu_i^H, \sigma_i^H\}$ and evaluate the fitness according to squared error function in Equation (4.2). It then repeatedly modifies the population of individual

solutions based on the concept of natural selection to elect best individuals and use them as parents to produce the next generation. A total of 150 iterations was sufficient to achieve convergence. The fitting is insensitive to the initial guesses and consistently converges to similar results.

3.5 Results of grid indentation

Impressions from indentation tests performed at 100 nm depth could not be detected through SEM imaging; therefore, a small grid of 3 × 2 indentations is performed at deeper penetration (200 nm) to visually demonstrate the grid indentation method on the NMC cathode. The residual impressions of such test is indicated in Figure 3.5.

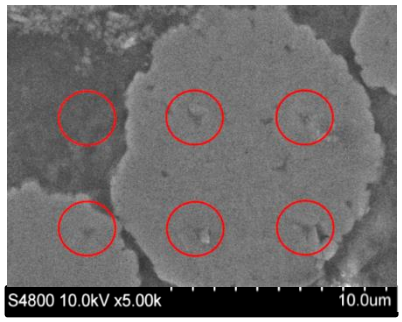

Figure 3.5. Example of a small indentation grid on NMC; imprints from indentations performed at 200nm depth (the mechanical properties are obtained with an indentation depth of 100 nm).

Figure 3.6 shows the distribution maps of elastic modulus and hardness generated from 121 tests in a 33μm × 33μm area. An excellent match between the mechanical properties and the phase distribution in the optical image is clearly seen – higher values are shown on NMC particles (stiff and hard) and lower values in the CB/PVDF matrix (compliant and soft). In addition, due to the small size of the particles embedded in the

matrix, a significant fraction of the data exhibit mixed properties of the particles and the matrix. Such mixed regions are referred as interface, the third constituent phase of the composite electrode in the light of the mechanical properties. The interface would exhibit a large variation in elastic modulus and hardness within the limits of the properties of NMC particles and CB/PVDF matrix. Figure 3.6b and Figure 3.6c enables an estimation of the range of the mechanical properties for each phase. For example, the contours show that the modulus of the particles are in between 120 and 160 GPa, while the modulus of the matrix lies within 0.1 and 10 GPa.

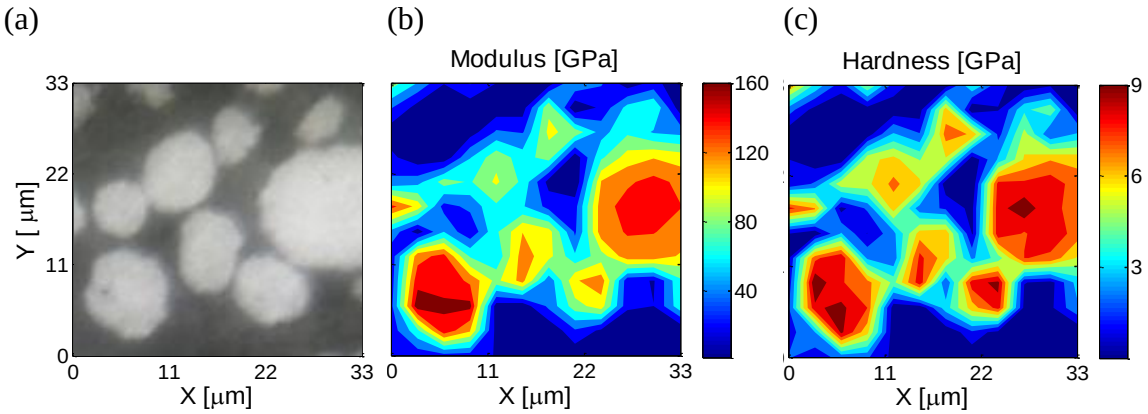

Figure 3.6. (a) Optical image of a 33μm × 33μm area for grid indentation. Contour plot of (b) elastic modulus and (c) hardness in the selected area.

The results of grid indentation tests are analyzed using the statistical procedure described earlier in order to extract the mechanical properties of the NMC particles, CB/PVDF matrix, and the interface. Figure 3.7a and Figure 3.7c shows the results of the fitting of experimental CDFs of elastic modulus and hardness properties using a tri-modal Gaussian distributions. The corresponding experimental PDFs using the same set of parameters as in the CDFs fitting are presented in Figure 3.7b and Figure 3.7d. The estimated elastic properties of the NMC 532 and CB/PVDF phases are, respectively, 123

GPa and 4.4 GPa. The PDFs of the hardness measurements displayed more well-defined peaks as compared with measurements of the elastic modulus. Consequently, a better CDF curve fitting is obtained for the hardness property. This is consistent with the work of Randall et al. [59], which also found that the grid indentation method provides a better estimation of the hardness than of the modulus. The estimated hardness of the NMC and CB/PVDF phases are, respectively, 7.78 GPa and 0.13GPa. The grid indentation results are validated in the next section.

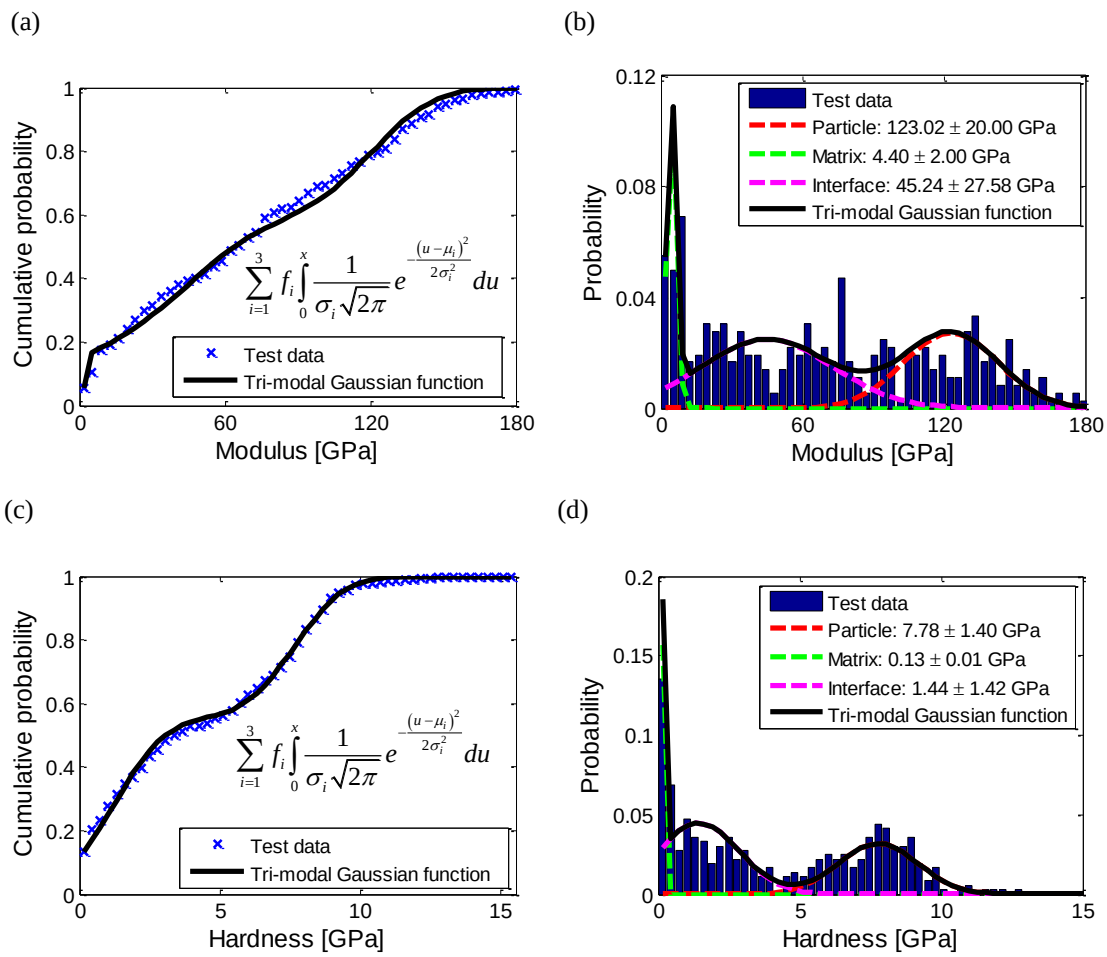

Figure 3.7. (a) Cumulative probability of elastic modulus and tri-modal Gaussian fitting. (b) Plots of probability distribution function using the same set of parameters in (a). (c) Cumulative probability of hardness and tri-modal Gaussian fitting. (d) Plots of probability distribution function using the same set of parameters in (c).

3.6 Validation through selective indentation

In order to validate grid indentation results, the mechanical properties of the NMC active particles and the PVDF/CB are investigated through two different approaches. The properties of the NMC phase are measured through indentation tests performed at the NMC particles only, as shown in Figure 3.8. Only particles of diameter larger than 10 μm are selected for this test in order to minimize the influence of the matrix properties. Tests are performed at indentation depths ranging from 50 nm up to 400 nm so as to evaluate the influence of the substrate - deeper indentations will be more influenced by the substrate properties than shallower indentations. The indentation sites can be specified precisely as a result of careful calibration of the stage XY coordinates relative to the optical microscope and indenter. The accuracy of the indentation location was verified by analyzing the impressions left from tests performed at deep indentations (400 nm penetration depth) as shown in Figure 3.8.

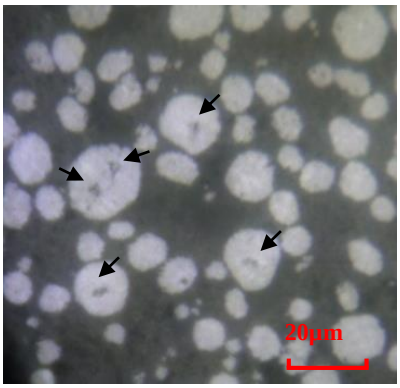

Figure 3.8. Optical image of selective indentation impressions on NMC particles at 400nm maximum penetration

The selective indentation approach is not effective in the characterization of the CB/PVDF phase; the irregular shape of the CB/PVDF phase makes it impossible to

distinguish if there is NMC particles buried only a few nanometers underneath the CB/PVDF coating. As a result, in order to validate the matrix phase properties obtained by grid indentation, samples composed of the only CB/PVDF were fabricated and tested. These samples were prepared maintaining the same CB and PVDF weight ratios as in the NMC electrode (Table 3.1).

Table 3.1. Sample composition

	NMC [wt%]	PVDF [wt%]	CB [wt%]
NMC cathode	90	5	5
PVDF/CB sample	0	50	50

The mechanical property measurements on the matrix may be affected by its porosity. Thus, the porosity, ε, was calibrated by measurements of weight, surface area, and thickness of samples consisting of composite electrode and current collector by the following equation:

$$\varepsilon = \frac{V_m - V_t}{V_m} = \frac{A_s h_s - (w_s - A_s h_{Al} \rho_{Al}) \left(\frac{f_{NMC}}{\rho_{NMC}} + \frac{f_{PVDF}}{\rho_{PVDF}} + \frac{f_{CB}}{\rho_{CB}} \right)}{A_s h_s}, \qquad (4.4)$$

where the volume of the electrode (excluding the Al current collector) is $V_m = A_s h_s$, and the theoretical volume of zero porosity is V_t. A_s is the surface area, h_{Al} and h_s are the thickness of the Al substrate and the electrode, respectively. w_s represents the sample weight and f the weight fraction of individual components. The theoretical density (ρ) of NMC, CB, PVDF, and Al foil are, respectively, 4.77, 1.90, 1.76 and 2.70 mg/mm^3.Table 3.2 lists the parameters used to calibrate the porosities of three samples of NMC electrode and CB/PVDF. The average porosities are 61% for CB/PVDF and 56% for NMC cathode.

Table 3.2. Porosity calibration of CB/PVDF and NMC electrode samples

Sample	CB/PVDF			NMC electrode		
	1	2	3	1	2	3
A_s [mm^2]	145.81	712.09	174.85	2886.65	1179.34	591.46
h_s [μm]	17.74	17.74	17.74	56.93	55.33	57.26
h_{Al} [μm]	16.57	16.57	16.57	0.015	0.015	0.015
w_s [mg]	1.47	6.67	7.49	418.64	166.13	83.60
ε [%]	61.39	63.71	57.95	55.32	55.86	57.15

The results of the characterization of the NMC 532 phase are first presented. Figure 3.9a shows the load-displacement curves from tests performed at different penetrations displaying typical metal behavior. Load-displacement curves from tests performed at 400nm occasionally displayed small pop-in events during loading, suggesting that cracks start to form beyond such indentation depth. Figure 3.9b shows the distribution of elastic modulus and hardness at maximum indentation depths of 50, 100, and 150 nm. The test data obey an approximately Gaussian distribution with relatively small deviation, which suggests that the indentations are indeed performed within the particles. The measured properties of the NMC particles are sensitive to the maximum indentation depth due to the effect of particle microstructure at shallow indentation and the effect of surrounding CB/PVDF medium at deep indentation. Figure 3.9c shows the dependence of the measured modulus and hardness on the maximum indentation depth in the range of 50 nm to 420 nm. The red spots indicate mean values and error bars indicate the corresponding standard deviations. The region marked in the blue rectangles represents the optimum indentation depth to measure the intrinsic properties of NMC particles. Results below 75 nm are likely to be influenced by surface features of the particles and instrument precision limitations. At the other end, indentations performed over 150 nm are more strongly affected by the

surrounding compliant medium, resulting in a gradually decreasing modulus and hardness at larger indentation depth. The average values of elastic modulus and hardness are 138.73 GPa and 8.89 GPa, respectively, in the optimum window of indentation depth ranging from 75 nm to 150 nm.

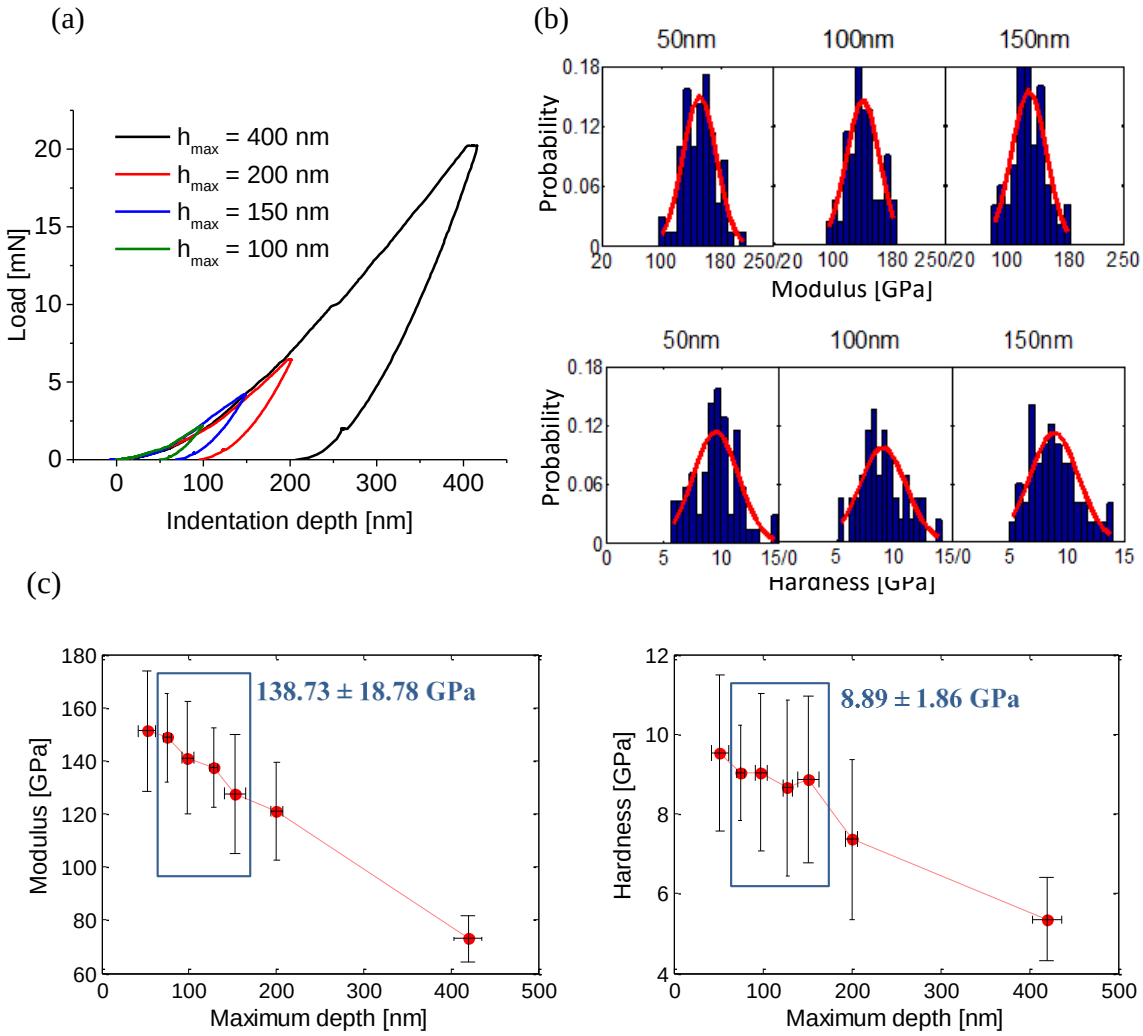

Figure 3.9. Experimental results of selective indentation on NMC particles. (a) Typical load-displacement curve of nanoindentation and (b) Indentation histograms of elastic modulus and hardness for 50nm, 100nm and 150nm maximum indentation depth. (c) Dependence of elastic modulus and hardness on the maximum indentation depth. The blue rectangles mark the range in which the measured properties are less sensitive to the effect of particle microstructure at shallow indentation and the effect of surrounding medium at deep indentation.

Similar tests are performed on pure CB/PVDF samples to evaluate the mechanical properties at various indentation depths. A total of 350 tests are carried out at different sites. The maximum indentation depth should be chosen to avoid the effect of surface roughness at shallow indentation and the effect of aluminum foil substrate at deep indentation. Figure 3.10 shows the elastic modulus and hardness for indentation tests ranging from 200 nm to 2200 nm depth. The mechanical properties are relatively insensitive to the indentation depth and the average values of elastic modulus and hardness are 1.78 GPa and 0.043 GPa, respectively. It is worth noting that the mechanical properties of the CB/PVDF samples may vary with the porosity value – the tested samples have a porosity of 61%. One may expect to obtain higher values of elastic modulus and hardness for samples of lower porosity.

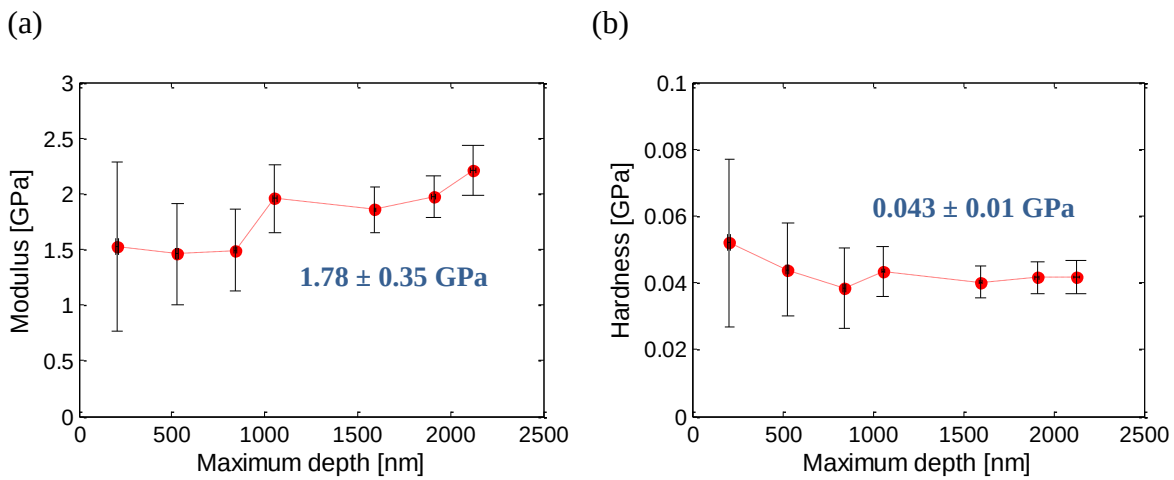

Figure 3.10. (a) elastic modulus and (b) hardness of CB/PVDF sample measured at various indentation depths. The mechanical properties are relatively insensitive to the effect of surface roughness at shallow indentation and the substrate effect at deep indentation

3.7 Discussion

Table 3.3. summarizes the surface fractions, mean and standard deviation of elastic modulus and hardness obtained from the statistical analysis and its comparison with results from selective indentation tests. The mechanical properties of the NMC particles determined by grid indentation and selective indentation are in good agreement. For the CB/PVDF matrix, however, grid indentation yields larger values of modulus and hardness by a factor of 2~3. The more accurate estimation of the properties of the NMC phase as compared to the estimation of the properties of the CB/PVDF phase was indeed expected; the larger size and uniform spherical shape of the NMC particles enables more tests to measure single phase properties, facilitating the statistical deconvolution process. The difference found in the matrix properties is mostly due the high incidence of tests affected by NMC particles buried underneath the surface of CB/PVDF coating. Overall, the slight underestimation of the NMC properties and more substantial overestimation of the matrix property indicate that the indentation depth employed is not able to completely eliminate the substrate effect. However, this comparison may not be unreasonable given the complexity of the microstructure and the large difference in the mechanical properties of the material phases in the composite.

Table 3.3. Surface fractions, elastic modulus, and hardness of individual components determined by grid indentation and selective indentation.

Material Phase	Surface fraction [%]	Modulus [GPa] ($\mu \pm \sigma$)		Hardness [GPa] ($\mu \pm \sigma$)	
	Grid Ind.	Grid Ind.	Sel. Ind.	Grid Ind.	Sel. Ind.
Particles	38.40	123.02 ± 20	138.73 ± 18.78	7.78 ± 1.40	8.89 ± 1.86
Matrix	15.64	4.40 ± 2	1.78 ± 0.35	0.13 ± 0.01	0.043 ± 0.01
Interface	45.96	45.24 ± 27.58		1.44 ± 1.42	

3.8 Conclusions

The combinatory technique of grid indentation and statistical deconvolution provides a fast and practical route to determine the mechanical properties of heterogeneous materials that can feed the constitutive models of composite electrodes. Compared against other methods such as selective indentations at targeted phases or fabrication of bulk samples, the grid indentation method is far less labor intensive and it allows the characterization of multiple materials at once with little post processing. However, special attention should be paid to the ratio between indention depth and characteristic size of constituents; accuracy of the fitting strongly depends on this factor. Overall, the grid indentation technique coupled with statistical deconvolution serves as a valuable tool in the characterization of mechanical behaviors of commercial electrodes as well as in the design of high-performance rechargeable batteries.

4. IN-SITU NANOINDENTATION

4.1 The need of in-situ technique

The mechanical properties of active materials in LIBs vary significantly with Li concentration [71] [72]. In high-capacity electrodes, such as Si anode and S cathode, Li concentration varies substantially, inducing a dramatic change in the mechanical properties of the lithiated phases [73] [74] [75]. The evolution of mechanical properties demonstrates a transition from the brittle material to a highly ductile behavior in the course of lithiation. The elastic modulus of graphite, for instance, changes by a factor of three during lithiation [76] and the elastic modulus of $LiMn_2O_4$ cathode gradually increase from 87 GPa at 0% SOC (pristine state) to 104 GPa at 100% SOC (fully lithiated state) [77].

Knowledge of the mechanical properties of active materials as a function of Li concentration is critical in the development of reliable models of deformation and fracture mechanics for Li-ion batteries. Also, the direct correlation between mechanical stability and electrochemical performance provides valuable information for the rational design of high-capacity electrodes.

Measuring the mechanical properties as a function of the state of charge is challenging task for multiple reasons. For instance, the lithiated electrodes and electrolyte in Li-ion cells are extremely sensitive to the environment; contamination can be induced by traces of oxygen and moisture. In contact with water, $LiPF_6$ salt in the electrolyte

decomposes and hydrolyzes to form HF. HF may react with the active material in the positive electrode causing partial dissolution and forming more water molecules that continues to decompose $LiPF_6$ salt [78] [79]. Most mechanical testing facilities are, however, open system with bare environment control. This lack of environmental control induces a considerable scatter and inconsistencies in the data due to alterations in the surface properties of the sample as well as in the electrochemical performance of the battery. Therefore, an experimental platform that allows in-situ mechanical characterization of electrode materials is urgently needed.

In-situ nanoindentation presents multiple challenges such as dealing with limited indentation axis travel range, requiring an inert environment, dealing with volumetric expansion, electrolyte evaporation and SEI layer, and finally, dealing with space constraints - fluid cell design has to accommodate all crucial test components including optics, indenter, electrodes, electrolyte, and potentiostat probes.

This section presents the development of an in-situ mechanical characterization platform that overcomes all the practical issues mentioned earlier. First, the apparatus design and implementation is presented. Then, the experimental procedure used to characterize a silicon thin film as a function of the state of charge, including general considerations regarding in-situ tests, is described. Finally, the test results are presented and compared with literature data.

4.2 Materials and methods

In order to perform experiments under inert atmosphere, the indenter is placed inside an Argon filled glovebox with controlled oxygen and water concentrations below

0.5 ppm. The Keysight G200 nanoindenter is employed for mechanical characterization and the VersaSTAT 3 potentiostat for electrochemical analysis. All cables are potted to connect with outside controller. A special three-electrode electrochemical cell is designed to enable indentation and electrochemical analysis to take place simultaneously. The experimental setup is summarized in Figure 4.1.

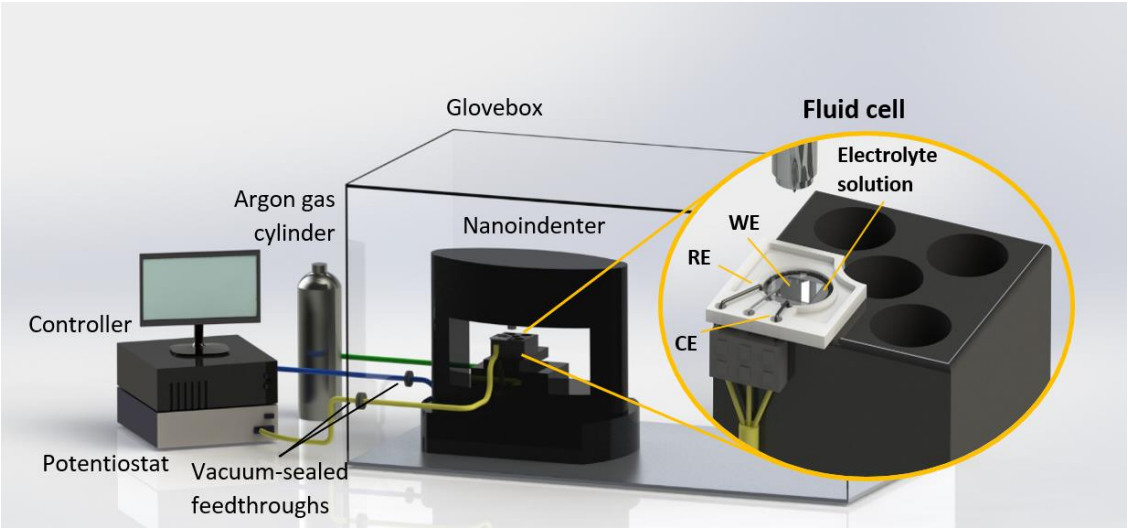

Figure 4.1. In-situ nanoindentation platform

The fluid cell is a key in the design of the in-situ platform. Figure 4.2 shows a picture of the fluid cell containing the sample in the middle as the working electrode (green clip), a lithium ribbon as the counter electrode (red clip) wrapped around the perimeter, and a smaller lithium ribbon as the reference electrode (white clip). The equipment used in this work has a maximum indenter travel distance (vertical direction) of only 1500 µm. The sample height relative to the fluid cell can be adjusted to allow complete immersion of the sample in the electrolyte, leaving a layer of approximately 800 µm over its surface. The fluid cell has a fixed height relative to the stage and a flat surface below the tip travel path, so that the indenter is allowed to travel safely when automatically exchanging to and

from microscope mode. Maintaining this capability is crucial in order to evaluate the surface quality before tests and to select desired test locations with precision. The liquid cell is connected to a potentiostat that charges or discharges the battery cell. The state of charge is obtained by monitoring the lithiation capacity. Nanoindentation is continuously performed on the surface of the working electrode simultaneously with lithiation or delithiation.

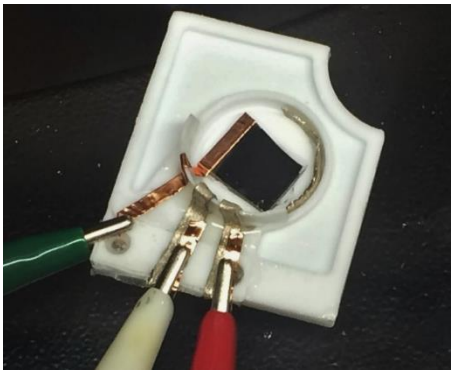

Figure 4.2. Three electrode fluid cell showing the working electrode connected by copper tape to the sample (green), counter electrode (red) to a long lithium ribbon, and reference electrode (white) connected to short lithium ribbon.

The presence of the $LiPF_6$-PC electrolyte did not influence measurements, as it can be verified from tests performed for dry and wet amorphous silicon, Table 4.1.

Table 4.1. Comparison between tests performed on dry sample and completely immersed sample.

Material	# tests	h_{max} [nm]	Fluid	Modulus [GPa]	Hardness [GPa]
Amorphous Silicon	9	100	Dry	92.19	7.65
	9	100	$LiPF_6$-PC	92.33	7.76

4.3 Preliminary results

4.3.1 Silicon overview

Silicon electrodes offer a chance for huge improvement in the capacity of current anode materials. The practical specific capacity up to 3579 $mAhg^{-1}$ of silicon compared to 372 $mAhg^{-1}$ of graphite, represents an increase in Li storage per weight of nearly 10 times [75]. This increase in Li storage comes at a cost of large volumetric changes of 280% upon full lithiation. This volumetric change induces large stresses in the material, leading to mechanical degradation and capacity loss. Mechanical degradation and the resultant capacity fade in silicon limits its employment in high-performance rechargeable batteries. As a result, numerous studies have been carried out in the past years with the goal of better understanding the details of the lithiation behavior of Si [40] [74] [80] [81].

The mechanical properties of silicon vary substantially with the SOC. For amorphous silicon, the elastic modulus range from 90 to 100 GPa and hardness from 5 to 10 GPa, while for fully lithiated silicon ($Li_{\sim 3.6}Si$), they range from 10 to 40 GPa for the elastic modulus and from 1.3 GPa to 1.8 GPa for the hardness [35] [82] [83] [84].

Despite intensive investigation, most data available on the hardness and modulus of lithiated silicon rely on ex-situ tests and provide the information only at a few Li concentrations with significant scatter. The variation between reported measurements can be attributed to differences in the experimental procedures employed. For example, one study performs measurements after the sample has been removed from the coin cell [83], while another performs perform measurement with the sample immersed in electrolyte, however, the sample is too thin to avoid substrate effect [82]. The technique proposed in this work allows for faster and more reliable data acquisition than the currently available

methods. The most relevant data in the literature are compared against the in-situ measurements in this work.

4.3.2 Sample preparation

The Si thin-film electrode is prepared using a DC magnetron sputtering system. A 50 nm Ti thin film was first sputtered for 5 min from a Ti target (50.8 mm diameter) onto a 175 μm thick glass substrate at 100 W power and at a pressure of 3 mTorr of argon. A 300 nm copper film was then deposited for 15 min from a Cu target (50.8 mm diameter) on the Ti underlayer at 200 W power and at a pressure of 5 mTorr of argon. The Cu film serves as the current collector, and the Ti underlayer is used to improve the adhesion between the Cu film and the glass substrate. A 500 nm Si film was subsequently deposited for 33 min from a Si target (50.8 mm diameter) at 100 W power and at a pressure of 5 mTorr of argon. Sample main dimensions are indicated in Figure 4.3.

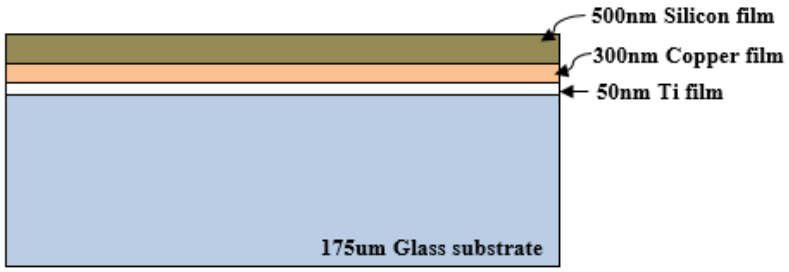

Figure 4.3. Sample dimensions

4.3.3 Electrolyte

1M $LiFP_6$-PC electrolyte is selected for this study. Depending on the electrolyte and test time, solvent evaporation can considerably lower fluid level and change salt concentration in the cell. $LiFP_6$-PC has the advantage of being nonvolatile. Also, it offers

a low surface tension, which prevents capillarity from pulling fluid up into indenter column. This eliminates the need for any special tip design, which could potentially interfere with the load frame stiffness, reducing the maximum usable load.

4.3.4 Test setup

The cell is discharged at a constant current of 0.02 mA until the potential reaches 0.01 mV vs Li^+/Li. Indentation tests are continuously performed throughout the discharge process, resulting in a total of 227 data points. In addition, 16 indentations are performed at open circuit (OC) before lithiation (pure silicon) and after full lithiation (~$Li_{3.7}Si$). A Berkovich tip is employed and indentations are performed at a maximum penetration depth of 100 nm. Substrate properties are not expected to significantly influence results since the maximum indentation depth selected corresponds to 20% the thickness of the thin film, as discussed in Section 2.3.4. Tests are performed at a constant strain rate of 0.05 s^{-1} with a peak hold time of 60 s to allow the material to creep before unloading. A constant Poisson ratio of 0.22 is chosen for all tests.

4.3.5 Volume expansion due to lithiation

The transient nature of test itself is challenging to nanoindentation tests. During lithiation, the silicon thin film will expand in the vertical direction, resulting in an inaccurate measurement of the indentation depth that can potentially lead to an overestimation of the mechanical properties. Nevertheless, drift caused by volumetric expansion could, in theory, be eliminated or at least minimized by the thermal drift correction. As explained in the nanoindentation chapter, thermal drift correction is applied

to account for thermal expansion and electronic drift. The longer the test, that is, the slower the loading/unloading time, the more influence the drift has on the results. The drift in the thickness of the sample is calculated considering a 370 % volume expansion at maximum capacity of 3579 mAh/g. A one-dimensional expansion is expected for thin films - the thickness varies with lithiation while the area parallel to the substrate is kept constant. Hence, the volumetric expansion ratio is equal to the thickness expansion ratio. The linear relationship between film thickness and consumed capacity is given by $h_f = h_i(1 + 2.7z)$, where z is the capacity ratio and h_f and h_i are initial and final film thickness, respectively [85] [86]. Hence, the drift rate sensed by the indenter during cell discharge (Si lithiation) at constant current is given by:

$$\text{Drift rate due to lithiation} \cong \frac{2.7 * z * h_i}{t}, \tag{5.1}$$

where t is the total discharge time. Hence, the drift rate at a C-rate of 1/29 is $0.012\ nm/s$. This value lies within the range of the drift rate measured in standard tests on dry samples (0.1 - 0.005 nm/s). The drift rate is corrected by the procedure presented in Section 2.3.2. The effectiveness of the correction depends on the drift rate being approximately constant during the indentation.

4.3.6 Residual stress

The residual stress in the sample after lithiation is another factor to take into consideration, which may affect indentation results. The film initially is likely stressed as a result of the sputtering process. As lithium becomes to be inserted into the electrode, the stress becomes compressive and keeps rising until it begins to flow plastically

approximately at a concentration of $Li_{0.4}Si$ [34]. Upon further lithiation, a continuous small reduction in the stress is observed until it reaches a value of approximately 450 MPa at a composition of $Li_{3.75}Si$ [34]. Residual stresses alone do not affect mechanical property measurements from nanoindentation tests; however, it can facilitate pile up [87]. As mentioned in Section 2.3.3, the Oliver and Phar method used to derive the mechanical properties is based on the assumption that the material behaves like an elastic half space penetrated by a rigid punch and, therefore, doesn't account for pile up. If pile up takes place, then the actual contact area will be bigger than the contact area estimated in Equation (2.8), leading to an overestimation of the elastic modulus and hardness. Whether or not pile-up is expected to take place is discussed later in Section 4.4 by analysis of the resulting load-displacement curves.

4.3.7 SEI layer formation

SEI layer formation was investigated through AFM measurements by Yoon et al. [88] for the same cell configuration used in the current study – amorphous silicon/$LiPF_6$-PC electrolyte/lithium metal. In the first discharge, the SEI layer growth becomes apparent after 1 V. The average thickness by the end of the discharge (0.1V) ranges between 2 to 3 nm, as shown in Figure 4.4. This value is less than 4% the selected indentation depth of 100 nm and, therefore, the SEI layer should not to interfere significantly with measurements. If thicker SEI layer was the case, then deeper indentations could be employed to maintain the ratio between the SEI layer and indentation depth below 5%, keeping the SEI layer properties interference negligible. The roughness is only increased

by 2 nm [88], corresponding to only 5% the maximum indentation depth, satisfying recommendations by ISO 15477 covered in Section 2.3.5.

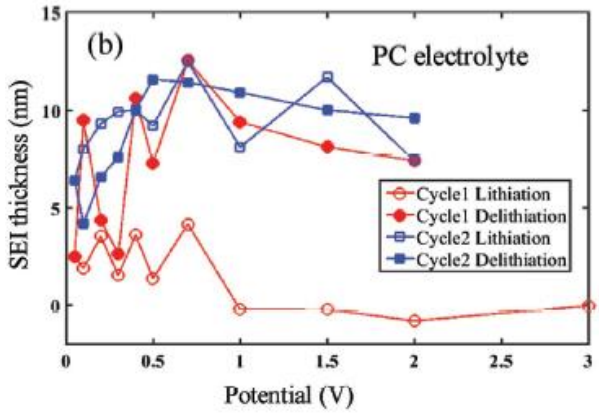

Figure 4.4. Thickness of SEI layer on silicon thin film as a function of equilibrium potential for 1.2M $LiPF_6$ in PC during the first two cycles [88].

4.4 Results and discussion

Mechanical and electrochemical analysis were performed simultaneously on a three electrode cell configuration, composed of amorphous silicon and lithium metal, in a $LiPF_6$-PC electrolyte solution. The electrochemical profile for lithium insertion into amorphous silicon during the first galvanostatic discharge is shown in Figure 4.5. The low C-rate of approximately 1/29 should allow sufficient time for diffusive equilibrium across the film. The specific capacity at the cut-off potential of 0.01 mV was 3469 mAh/g.

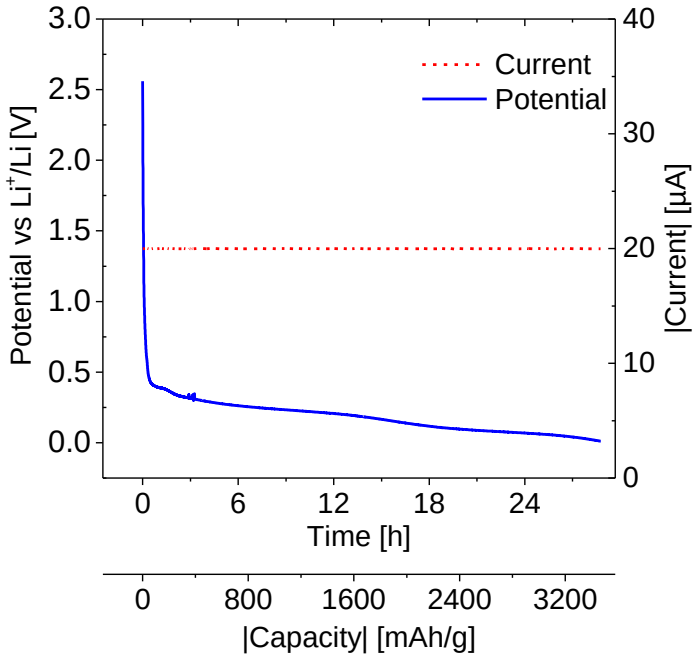

Figure 4.5. Electrochemical profile for lithium insertion into amorphous silicon (blue) and constant discharge current (red).

Figure 4.6 shows the measured mechanical properties as a function of the state of charge. Each point represents the result of one indentation test. It is noticeable that the results are highly consistent, following a smooth trend without apparent discontinuities. Pure lithium metal is softer than amorphous silicon, thus it was expected that both modulus and hardness will decrease with lithium content. The results from tests performed during galvanostatic discharge (red) and tests performed at open circuit (blue), at the beginning and at the end of the discharge, are practically the same, indicating that the rate of volume expansion was sufficiently low in order to not affect measurements. Figure 4.6a shows that the elastic modulus decreases linearly with capacity. This elastic softing is explained by considering the the charge-density and atomic bonding in lithiated alloys as predicted by DFT (density functional theory) calculations in the work of Shenoy et al. (2010). In Figure

4.6b, the hardness drops more steeply from pure silicon up to a Li concentration approximately equal to the Si concentration (LiSi), followed by a gradual decrease for further lithium insertion up to ~$Li_{3.7}Si$. The R-squared value indicates the quality of the fit, where R^2=1 represents a perfect fit. The fitted functions of the hardness and modulus (y= H(x) and E(x)) are given on the left-lower corner of Figure 4.6a and Figure 4.6b, respectively. This functions can be implemented in constitutive models in order to generate realistic predictions of mechanical behaviors in real silicon electrodes

(a) (b)

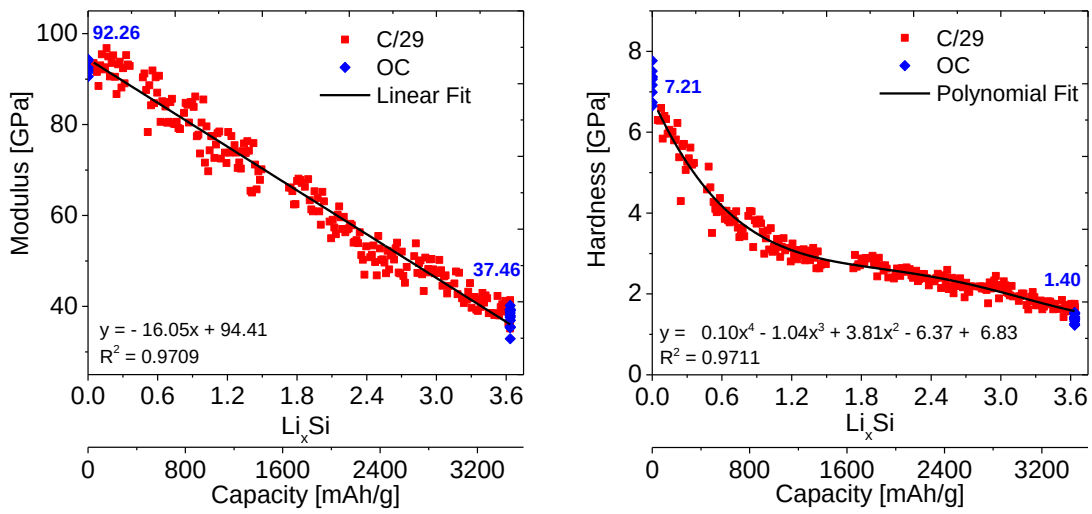

Figure 4.6. Nanoindentation tests performed during discharge (red) and during OC (blue). (a) elastic modulus and (b) hardness as a function of the capacity.

The elastic modulus was calculated assuming a constant Poisson ratio corresponding to the value of amorphous silicon (v=0.22). First-principles DFT studies have found evidence that the Poisson ratio is either independent [76] or fluctuates very little with Li concentration [75]. Other studies assume that the Poisson ratio obeys the general rule of mixture: $v(x_{Li}) = v_{host} * (1 - x_{Li}) + v_{Li} * x_{Li}$, where v and x are,

respectively, the Poisson ratio and the fraction of atoms [35] [84]. The elastic property measured by nanoindentation is not significantly affected by the estimated Poisson ratio. This is verified by comparing results showed previously where the Poisson ratio is considered to be constant (v=0.22) versus calculations assuming a linear variation of v between that of pure silicon ($v_{Si} = 0.22$) and that of pure lithium ($v_{Li} = 0.36$). The overall difference in the elastic moduli calculated for both scenarios is not significant, as presented in Figure 4.7.

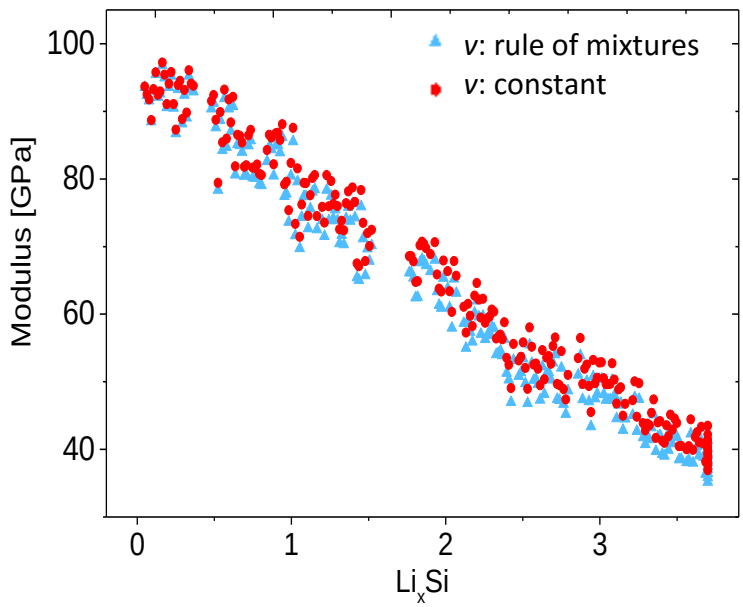

Figure 4.7. Elastic modulus assuming constant Poisson ratio with lithiation (red) and variable Poisson obeying the rule of mixtures (blue).

The load-displacement curves from tests performed at different ranges of the state-of-charge (SOC) are grouped and presented in individual plots in Figure 4.8. It can be observed that the load-displacement curves are fairly consistent within each range and do not show any obvious sign of crack or creep. Notice that the maximum load drops by half

its value during the first 30% of the discharge (roughly from 2 mN to 1 mN), compared by a drop of less than half its value during the rest of the 70% discharge. This explains the steep drop in the hardness properties observed in Figure 4.5b during the same capacity range, followed by a more gradual softening.

As covered in Section 2.3.3, the probability of pile-up can be estimated from the ratio between final indentation depth and maximum indentation depth (h_f/h_{max}) and the tendency of the material of work harden. A strong indication that the material is not to exhibit significant pile up is if h_f/h_{max}< 0.7, whether or not the material work hardens. Looking at the load-displacement curves below, it is possible to see that the h_f/h_{max} ratio ranges from roughly 0.6 for tests on pure silicon up to roughly 0.7 for tests on fully lithiated silicon. Thus, one should not expect errors associated with pile-up.

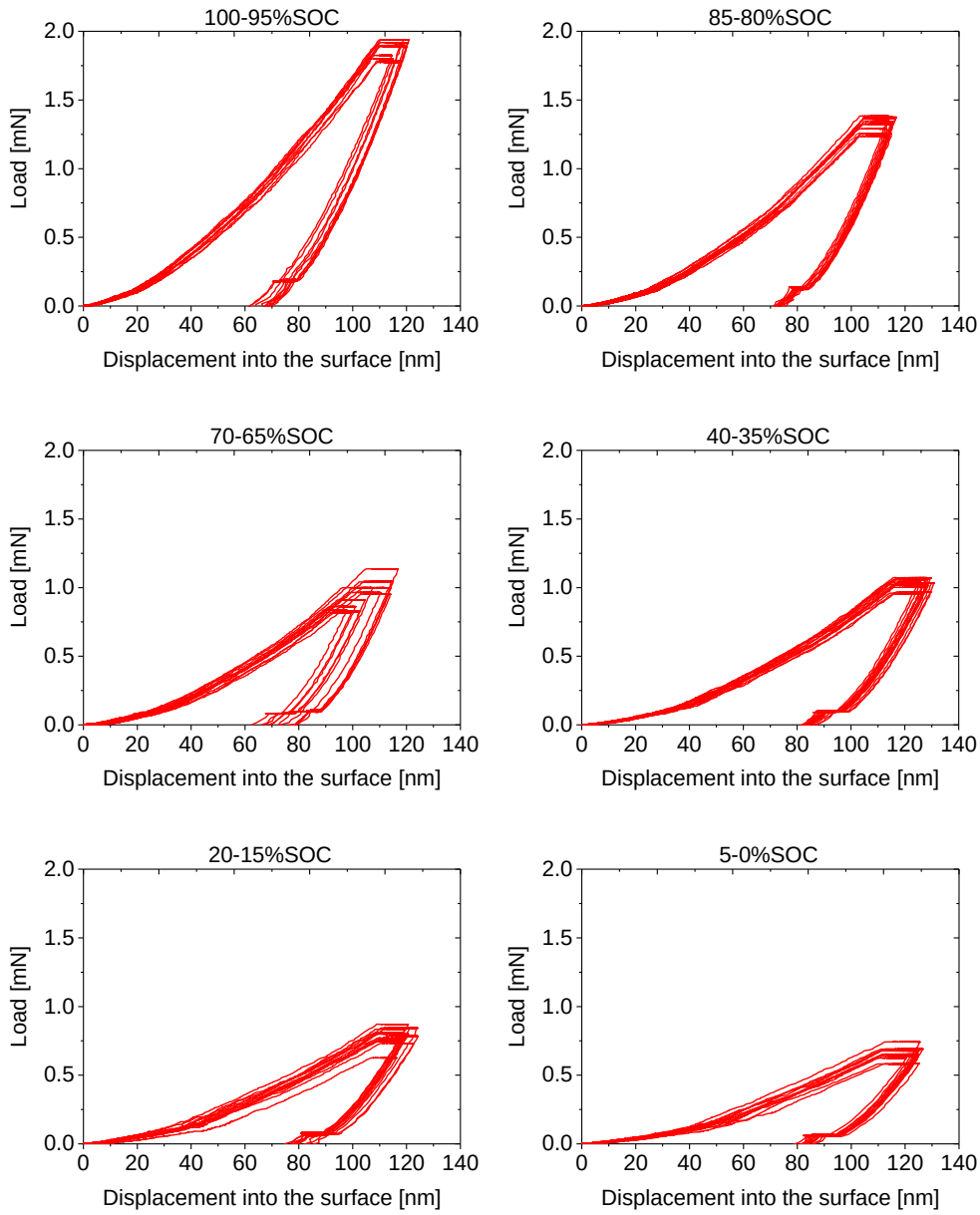

Figure 4.8. Batches of load-displacement curves obtained in different ranges of state-of-charge.

Figure 4.9a and Figure 4.9b show the same test data, however as a function of lithium fraction for comparison with theoretical and experimental literature data. The lithium fraction is given by $x/(x+1)$ in Li_xSi. It can be observed that the modulus

decreases mildly with lithium fraction, up until the composition of 50% lithium. Further lithiation leads to a slightly steeper decrease in the modulus properties and the properties of lithium start to dominate over the properties of silicon. This behavior is similar to the one observed by Berla et al. [84] shown in a black line. The hardness for pure amorphous silicon, 7.21GPa, decreases linearly as function of lithium fraction, down to 1.4 GPa at fully lithiated state ($Li_{0.78}Si_{0.22}$). Overall, our results are in reasonable agreement with literature data [75] [83] [84], in addition to being more detailed and showing a more consistent trend. Our approach also has the advantage of being high-throughput; in a single batch, with no interruptions, hundreds of data points are acquired and an accurate and continuous description of the mechanical properties dependence on lithium content can be achieved with a curve fitting.

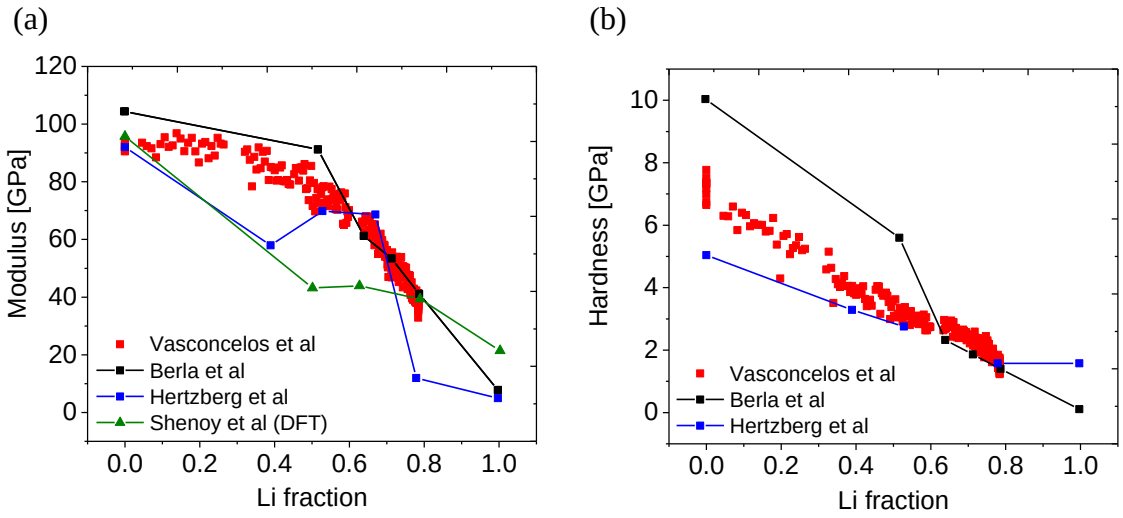

Figure 4.9. (c) Elastic modulus and (d) hardness as a function of Li fraction compared to results by Shenoy et al., [75] Hertzberg et al. [83] and Berla et al. [84].

4.5 Summary

In summary, an in-situ mechanical characterization platform consisting of a nanoindenter, a fluid cell, and a potentiostat are integrated inside a glovebox. The closed system prevents contamination from air and moisture and does not require removing the electrode from the fluid cell to perform indentation tests. In fact, indentation tests can be performed during slow charging or discharging without compromising the accuracy of the measurements. The fluid cell design allows full capability of the nanoindenter including using the microscope to evaluate the sample surface before running tests. Preliminary results are generated for silicon thin film. Overall the test data is highly consistent and it is in agreement with literature data. Young's modulus is found to decrease linearly with the state-of-charge (Li_xSi), from 92.3 GPa at 0% SOC (Si) to 37.5 GPa at 100% SOC ($Li_{3.7}Si$). Hardness, on the other hand, decreases linearly with lithium fraction ($Li_{x/(1+x)}Si$), obeying the general rule of mixtures, from 7.21 GPa at 0% SOC to 1.40 GPa at 100% SOC. This high-throughput approach allows testing hundreds of different Li concentrations automatically. In conclusion, this real time electrochemical and mechanical characterization enables practical and reliable quantitative analysis of electrochemically-induced changes in the mechanical properties of electrode materials.

5. CONCLUSIONS AND OUTLOOK

This thesis presented two mechanical characterization techniques for LIBs that allow for: (1) the characterization of multiple material phases in composite electrodes, and (2) measurement of the mechanical property evolution with the state-of-charge. The main conclusions are summarized below:

(1) Characterization of composite electrodes - the grid indentation technique coupled with statistical deconvolution was employed to measure the mechanical properties of individual constituents in a NMC cathode of high heterogeneity at the microscale. The extracted elastic modulus and hardness of the NMC particles and the surrounding CB/PVDF matrix are in good agreement with tests by selective indentation. Therefore, this combinatory technique provides a practical and reliable route to determine the mechanical properties of composite electrodes provided that the indentation depth is carefully chosen.

(2) In-situ characterization - an in-situ nanoindentation platform was designed, implemented and validated for simultaneous mechanical and electrochemical characterization of electrode materials. The technique overcomes practical issues related with environment requirements and instrument limitations, and enables comprehensive and consistent data acquisition. A preliminary study on silicon thin film was carried out to measure the mechanical properties dependence on lithium

concentration. Indentation tests performed during slow discharge are validated against indentation tests at open circuit and literature data. This high-throughput approach allows automatic characterization of hundreds of compositions across the entire range of lithiation without interruptions. Therefore, the in-situ nanoindentation technique serves as valuable tool in the characterization of mechanical behaviors of energy materials, as well as in the design of high-performance rechargeable batteries.

This thesis work focused on the development and validation of experimental tools that aid comprehensive mechanical characterization of electrode materials. In a future work, these tools will be employed in the rational design of electrode materials that mitigate mechanical degradation induced by lithiation. The investigation will allow for tuning active material composition to optimize performance in terms of capacity, cyclic rate, electrochemical stability, and lifetime. More specifically, the in-situ nanoindentation setup will be employed in the evaluation of mechanical properties of NMC electrodes as a function of the state-of-charge and in the course of electrochemical cycles. Finally, the relationship between mechanical property retention and capacity retention will be study in NMC electrodes with different compositions of Ni, Mn, and Co.

LIST OF REFERENCES

LIST OF REFERENCES

[1] M. Winter and R. J. Brodd, "What Are Batteries, Fuel Cells, and Supercapacitors?," *Chemical Reviews,* vol. 104, p. 4245−4269, 2004.

[2] J. Newman and K. E. Thomas-Alyea, Electrochemical Systems, Wiley-Interscience, 2004.

[3] A. J. Bard and L. R. Faulkner, Electrochemical Methods: Fundamentals and Applications, New York: Wiley, 2001.

[4] F. Scholz, "Thermodynamics of electrochemical reactions," in *Electroanalytical Methods,* Springer Berlin Heidelberg, 2010, pp. 11-31.

[5] G. D. Short and E. Bishop, "Concentration Overpotentials on Antimony Electrodes in Differential Electrolytic Potentiometry," *Analytical Chemistry,* vol. 37, no. 8, p. 962–967, 1965.

[6] G. G. Yadav, "Design and assembly of nanostructured complex metal oxide materials for the construction of batteries and thermoelectric devices," Doctoral dissertation, Purdue University, 2013.

[7] M. Ue, Y. Sasaki, Y. Tanaka and M. Morita, "Nonaqueous electrolytes with advances in solvents," in *Electrolytes for Lithium and Lithium-Ion Batteries*, Springer-Verlag New York, 2014, pp. 93-165.

[8] H. Zhao, S. -J. Park, F. Shi, Y. Fu, V. Battaglia, P. N. Ross and G. Liu, "Propylene carbonate (PC)-based electrolytes with high coulombic efficiency for lithium-ion batteries," *Journal of The Electrochemical Society,* vol. 161, no. 1, pp. A194-A200, 2014.

[9] J. C. Burns, A. Kassam, N. N. Sinha, L. E. Downie, L. Solnickova, B. M. Way and J. R. Dahn, "Predicting and extending the lifetime of Li-Ion batteries," *Journal of The Electrochemical Society,* vol. 160, no. 9, pp. A1451-A1456, 2013.

[10] T. Kawamura, S. Okadaa and J.-I. Yamaki, "Decomposition reaction of $LiPF_6$-based electrolytes," *Journal of Power Sources,* vol. 156, p. 547–554, 2006.

[11] S. S. Zhang, T. R. Jow, K. Amine and G. L. Henriksen, "$LiPF_6$-EC-EMC electrolyte for Li-ion battery," *Journal of Power Sources,* vol. 107, pp. 18-23, 2002.

[12] R. Petibon, L. Madec, D. W. Abarbanel and J. R. Dahn, "Effect of $LiPF_6$ concentration in $Li[Ni_{0.4}Mn_{0.4}Co_{0.2}]O_2$/graphite pouch," *Journal of Power Sources,* vol. 300, pp. 419-429, 2015.

[13] M. R. Palacin and A. de Guibert, "Why do batteries fail?," *Science,* vol. 351, no. 6273, p. 1253292, 2016.

[14] M. B. Pinson and M. Z. Bazant, "Theory of SEI formation in rechargeable batteries: capacity fade, accelerated aging and lifetime prediction," *Journal of The Electrochemical Society,* vol. 160, no. 2, pp. A243-A250, 2013.

[15] P. Verma, P. Maire and P. Novák, "A review of the features and analyses of the solid electrolyte interphase in Li-ion batteries," *Electrochimica Acta,* vol. 55, pp. 6332-6341, 2010.

[16] D. P. Abraham (Ed.), "Diagnostic examination of Generation 2 lithium-ion cells and assessment ofperformance degradation mechanisms," Argonne National Laboratory, Oak Ridge, TN, Rep. ANL-05/21, Jul. 2005.

[17] I. Laresgoiti, S. Kabitz, M. Ecker and D. U. Sauer, "Modeling mechanical degradation in lithium ion batteries during cycling: Solid electrolyte interphase fracture," *Journal of Power Sources,* vol. 300, pp. 112-122, 2015.

[18] R. Xu and K. Zhao, "Mechanical interactions regulated kinetics and morphology of composite electrodes in Li-ion batteries," *Extreme Mechanics Letters,* 2015.

[19] G. Ning, B. Haran and B. N. Popov, "Capacity fade study of lithium-ion batteries cycled at high discharge rates," *Journal of Power Sources,* vol. 117, no. 1-2, pp. 160-169, 2003.

[20] K. Jalkanen, J. Karppinen, L. Skogström, T. Laurila, M. Nisula and K. Vuorilehto, "Cycle aging of commercial NMC/graphite pouch cells at different temperatures," *Applied Energy,* vol. 154, p. 160–172, 2015.

[21] C. Birkl, "Degradation of lithium-ion batteries," Energy and Power Group, University of Oxford, 3 February 2014. [Online]. Available: http://epg.eng.ox.ac.uk/content/degradation-lithium-ion-batteries. [Accessed 6 May 2016].

[22] R. Hausbrand, G. Cherkashinin, H. Ehrenberg, M. Gröting, K. Albe, C. Hess and W. Jaegermann, "Fundamental degradation mechanisms of layered oxide Li-ion battery cathode materials: Methodology, insights and novel approaches," *Materials Science and Engineering B,* vol. 192, pp. 3-25, 2015.

[23] M. Ebner, F. Marone, M. Stampanoni and V. Wood, "Visualization and Quantification of Electrochemical and Mechanical Degradation in Li Ion Batteries," *Science,* vol. 342, pp. 716-720, 2013.

[24] D. Y. Wang, X. D. Wu, Z. X. Wang and L. Q. Chen, "Cracking causing cyclic instability of $LiFePO_4$ cathode material," *Journal of Power Sources,* vol. 140, no. 1, pp. 125-128, 2005.

[25] X. H. Liu, L. Zhong, S. Huang, S. X. Mao, T. Zhu and J. Y. Huang, "Size-Dependent Fracture of Silicon Nanoparticles During Lithiation," *ACS Nano,* vol. 6, no. 2, p. 1522–1531, 2012.

[26] P. Barai, V. P. Schulz and P. P. Mukherjee, "Analysis of mechanical degradation in lithium-ion battery electrodes," in *The Electrochemical Society meeting,* Cancun, Mexico, October 5 - October 9, 2014, Paper 447 MA2014-02.

[27] D. Chen, *Microscopic investigations of degradation in lithium-ion batteries,* Dr.-Ing. dissertation, Karlsruher Institut für Technologie, Karlsruher, Germany, 2012.

[28] A. Watanabe, M. Kinoshita, T. Hosokawa, K. Morigaki and K. Nakura, "Journal of Power Sources," *Capacity fading of $LiAl_yNi_{1-x-y}Co_xO_2$ cathode for lithium-ion batteries during accelerated calendar and cycle life tests (effect of depth of discharge in chargeedischarge cycling on the suppression of the micro-crack generation of $LiAl_yNi_{1-x-y}Co_xO_2$ particle),* vol. 260, pp. 50-56, 2014.

[29] X. H. Liu, Y. Liu, A. Kushima, S. Zhang, T. Zhu, J. Li and J. Y. Huang, "In Situ TEM Experiments of Electrochemical Lithiation and Delithiation of Individual Nanostructures," *Advanced Energy Materials,* vol. 2, p. 722–741, 2012.

[30] H. Sun, G. Xin, T. Hu, M. Yu, D. Shao, X. Sun and J. Lian, "High-rate lithiation-induced reactivation of mesoporous hollow spheres for long-lived lithium-ion batteries," *Nature Communications,* vol. 5, p. 4526, 2014.

[31] Toho Technologies., "Metrology Products," [Online]. Available: http://www.tohotechnology.com/flx-series.php#Theory. [Accessed 7 June 2016].

[32] G. Janssena, M. Abdallab, F. van Keulenc, B. Pujadad and B. van Venrooy, "Celebrating the 100th anniversary of the Stoney equation for film stress: Developments from polycrystalline steel strips to single crystal silicon wafers," *Thin Solid Films,* vol. 517, no. 6, p. 1858–1867, 6 Mar 2009.

[33] S. P. V. Nadimpalli, R. Tripuraneni and V. A. Sethuraman, "Real-Time Stress Measurements in Germanium Thin Film Electrodes during Electrochemical Lithiation/Delithiation Cycling," *Journal of The Electrochemical Society,* vol. 162 , no. 14, pp. A2840-A2846, 2015.

[34] M. Pharr, Z. Suo and J. J. Vlassak, "Measurements of the Fracture Energy of Lithiated Silicon Electrodes of Li-Ion Batteries," *Nano Letters,* vol. 13, p. 5570−5577, 2013.

[35] V. A. Sethuraman, M. J. Chon, M. Shimshak, N. Van Winkle and P. R. Guduru, "In situ measurement of biaxial modulus of Si anode for Li-ion batteries," *Electrochemistry Communications,* vol. 12, p. 1614–1617, 2010.

[36] Materials Evaluation and Engineering , "Tension and compression testing,", [Online]. Available: http://www.mee-inc.com/hamm/tension-and-compression-testing/. [Accessed 8 June 2016].

[37] C. Peabody and C. B. Arnold, "The role of mechanically induced separator creep in lithium-ion battery capacity fade," *Journal of Power Sources,* vol. 196, p. 8147–8153, 2011.

[38] J. Xu, B. Liu and D. Hu, "State of Charge Dependent Mechanical Integrity Behavior of 18650 Lithium-ion Batteries," *Scientific Reports,* vol. 6, no. 21829 , 2016.

[39] Y. Lu, Y. Ganesan and J. Lou, "A Multi-step Method for In Situ Mechanical Characterization of 1-D Nanostructures Micromechanical Device," *Experimental Mechanics,* vol. 50, p. 47–54, 2010.

[40] A. Kushima, J. Y. Huang and J. Li, "Quantitative Fracture Strength and Plasticity Measurements of Lithiated Silicon Nanowires by In Situ TEM Tensile Experiments," *American Chemical Society Nano,* vol. 6, no. 11, pp. 9425-9432, 2012.

[41] M. Z. Mughal, R. Moscatelli, H. -Y. Amanieu and M. Sebastiani, "Effect of lithiation on micro-scale fracture toughness of $Li_xMn_2O_4$ cathode," *Scripta Materialia,* vol. 116, pp. 62-66, 2016.

[42] M. Skrzypczak, C. Guerret-Piecourt, S. Bec, J.-L. Loubet and O. Guerret, "Use of a nanoindentation fatigue test to characterize the ductile–brittle transition," *Journal of the European Ceramic Society,* vol. 29, no. 6, p. 1021–1028, 2009.

[43] H. Lu, B. Wang, J. Ma, G. Huang and H. Viswanathan, "Measurement of Creep Compliance of Solid Polymers by Nanoindentation," *Mechanics of Time-Dependent Materials,* vol. 7, no. 3, pp. 189-207, 2003.

[44] V. Kuznetsov, A. -H. Zinn, G. Zampardi, S. Borhani-Haghighi, F. La Mantia, A. Ludwig, W. Schuhmann and E. Ventose, "Wet nanoindentation of the solid electrolyte interphase on thin film," *Applied Materials & Interfaces,* vol. 7, pp. 23554-23563, 2015.

[45] D. Tabor, "A simple theory of static and dynamic hardness," *Proceedings of The Royal Society,* vol. 192, no. 1029, pp. 247-274, 1947.

[46] Keysight Technologies, "How to Select the Correct Indenter Tip," 31 July 2014. [Online]. Available: http://literature.cdn.keysight.com/litweb/pdf/5990-4907EN.pdf?id=1791577. [Accessed 2016 June 2016].

[47] W. C. Oliver, "Measurement of hardness and elastic modulus by instrumented indentation: Advances in understanding and refinements to methodology," *Journal of Materials Research,* vol. 19, no. 1, pp. 3-20, 2004.

[48] Keysight Technologies, "Keysight Nano Indenter G200 User's Guide," Santa Rosa, CA, Rep. G2A-13192-1, Aug. 2014.

[49] A. Bushby, V. L. Ferguson and A. Boyde, "Nanoindentation of bone: Comparison of specimens tested in liquid and embedded in polymethylmethacrylate," *Journal of Materials Research,* vol. 19, no. 1, 2004.

[50] T. Chudoba and F. Richter, "Investigation of creep behaviour under load during indentation experiments and its influence on hardness and modulus results," *Surface and Coatings Technology,* vol. 148, no. 2–3, p. 191–198, 2001.

[51] J. Wheeler, D. Armstrong, W. Heinz and R. Schwaiger, "High temperature nanoindentation: The state of the art and future challenges," *Current Opinion in Solid State and Materials Science,* vol. 19, pp. 354-366, 2015.

[52] A. C. Fischer-Cripps, Introduction to Contact Mechanics, New York: Springer, 2007.

[53] *Standard Test Method for Vickers Hardness of Metallic Materials,* West Conshohocken, PA: American Society for Testing and Materials, 1987.

[54] K. Durst, M. Goken and H. Vehoff, "Finite element study for nanoindentation measurements on two-phase materials," *Journal of Materials Research,* vol. 19, no. 1, pp. 85-93, 2004.

[55] N. Conté and Anton Paar TriTec SA, "The Influence of Surface Roughness on Instrumented Indentation Testing (IIT)," [Online]. Available: http://www.anton-paar.com/?eID=documentsDownload&document=57427&L=23. [Accessed 30 June 2016].

[56] Keysight Technologies, "Indentation Rules of Thumb - Applications and Limits," 31 July 2014. [Online]. Available: http://literature.cdn.keysight.com/litweb/pdf/5990-5700EN.pdf?id=1888523. [Accessed 4 April 2016].

[57] J. Nohava, P. Haušild, Š. Houdková and R. Enžl, "Comparison of Isolated Indentation and Grid Indentation Methods for HVOF Sprayed Cermets," *Journal of Thermal Spray Technology,* vol. 21, no. 3, pp. 651-658, 2012.

[58] J. Nohava, P. Hausild, N. X. Randall and G. Favaro, "Grid nanoindentation on multiphase materials for mapping the mechanical properties of complex microstructures," in *IMEKO 2012 TC3, TC5 and TC22 Conferences, Metrology in Modern Context*, Pattaya, Chonburi, Thailand, 2010.

[59] N. X. Randall, M. Vandamme and F. -J. Ulm, "Nanoindentation analysis as a two-dimensional tool for mapping the mechanical properties of complex surfaces," *Journal of Materials Research,* vol. 24, pp. 679-690, 2011.

[60] G. Constantinides, K. S. Ravi Chandran, F.-J. Ulm and K. J. Van Vliet, "Grid indentation analysis of composite microstructure and mechanics: Principles and validation," *Materials Science and Engineering: A,* vol. 430, no. 1-2, p. 189–202, 2006.

[61] F. -J. Ulm, M. Vandamme, C. Bobko and J. A. Ortega, "Statistical Indentation Techniques for Hydrated Nanocomposites: Concrete, Bone, and Shale," *Journal of the American Ceramic Society,* vol. 90, no. 9, p. 2677–2692, 2007 .

[62] Amanieu, H. -Y, D. Rosato, M. Sebastiani, F. Massimi and D. F. Lupascu, "Mechanical property measurements of heterogeneous materials by selective nanoindentation: Application to LiMn2O4 cathode," *Materials Science & Engineering A,* vol. 593, p. 92–102, 2014.

[63] C. M. Julien, A. Mauger, K. Zaghib and H. Groult, "Comparative Issues of Cathode Materials for Li-Ion Batteries," *Inorganics,* vol. 2, 2014, pp. 132-154.

[64] T. Ohzuku and Y. Makimura, "Layered lithium insertion material of LiNi1/2Mn1/2O2 : A possible alternative to LiCoO2 for advanced lithium-ion batteries," *Chemistry Letters,* vol. 30, no. 8, pp. 744-745, 2001.

[65] M. M. Doeff, "Battery Cathodes," in *Batteries for Sustainability,* Springer New York, 2013, pp. 5-49.

[66] S. -M. Bak, E. Hu, Y. Zhou, X. Yu, S. D. Senanayake, S. -J Cho, K. -B. Kim, K. Y. Chung, X. -Q. Yang and K. -W. Nam, "Structural Changes and Thermal Stability of Charged $LiNi_xMn_yCo_zO_2$ Cathode Materials Studied by Combined In Situ Time-Resolved XRD and Mass Spectroscopy," *ACS Applied Materials and Interfaces,* vol. 6, no. 24, p. 22594–22601, 2014.

[67] J. Nanda, "Advances in Cathode Materials for High Energy Density Lithium-Ion Batteries," in *229th The Electrochemical Society Meeting,* San Diego, CA, May 29 – June 2, 2016, Paper 438 MA2016-01.

[68] D. Mohanty, K. Dahlberg, D. M. King, L. A. David, A. S. Sefat, D. L. Wood, C. Daniel, S. Dhar, V. Mahajan, M. Lee and F. Albano, "Modification of Ni-Rich FCG NMC and NCA Cathodes by Atomic Layer Deposition: Preventing Surface Phase Transitions for High-Voltage Lithium-Ion Batteries," *Scientific Reports,* vol. 6, p. 26532, 2016.

[69] J. Li, C. Daniel, S. An and D. Wood, "Evaluation residual moisture in lithium-ion battery electrodes and its effect on electrode performance," *MRS Advances,* vol. 1, no. 15, pp. 1029-1035, 2016.

[70] S. D. Sudhoff, "Genetic Optimization System Engineering Toolbox 2.6," 1 January 2014. [Online]. Available: https://engineering.purdue.edu/ECE/Research/Areas/PEDS/go_system_engineering_toolbox. [Accessed 6 December 2015].

[71] Y. Qi, L. G. Hector, C. James and K. J. Kima, "Lithium Concentration Dependent Elastic Properties of Battery Electrode Materials from First Principles Calculations," *Journal of The Electrochemical Society,* vol. 161, no. 11, pp. F3010-F3018, 2014.

[72] J. G. Swallow, W. H. Woodford, F. P. McGrogan, N. Ferralis, Y. -M. Chiang and J. Van Vliet, "Effect of Electrochemical Charging on Elastoplastic Properties and Fracture Toughness of Li_XCoO_2," *Journal of The Electrochemical Society,* vol. 161, no. 11, pp. F3084-F3090, 2014.

[73] F. Fan, S. Huang, H. Yang, M. Raju, D. Datta, V. B. Shenoy, A. C. T. van Duin, S. Zhang and T. Zhu, "Mechanical properties of amorphous Li_xSi alloys: a reactive force field study," *Modelling Simulation in Materials Science Engineering,* vol. 21, p. 074002, 2013.

[74] S. T. Boles, A. Sedlmayr, O. Kraft and R. Mönig, "In situ cycling and mechanical testing of silicon nanowire anodes for lithium-ion battery applications," *Applied Physics Letters,* vol. 100, p. 243901, 2012.

[75] V. B. Shenoy, P. Johari and Y. Qi, "Elastic softening of amorphous and crystalline Li-Si phases with increasing Li concentration: A first-principle study," *Journal of Power Sources,* vol. 195, pp. 6825-6830, 2010.

[76] Y. Qi, H. Guo, L. G. Hector and A. Timmons, "Threefold increase in the Young's modulus of graphite negative electrode during lithium intercalation," *Journal of Electrochemical Society,* vol. 157, no. 5, pp. A558-A566, 2010.

[77] H. -Y. Amanieu, M. Aramfard, D. Rosato, L. Batista, U. Rabe and D. Lupascu, "Mechanical properties of commerical $Li_xMn_2O_4$ cathode under different states of charge," *Acta Materialia,* vol. 89, pp. 153-162, 2015.

[78] M. Wohlfahrt-Mehren, C. Vogler and J. Garche, "Aging mechanisms of lithium cathode materials," *Journal of Power Sources,* vol. 127, p. 58–64, 2004.

[79] N. Wu, B. Feng, D. Yang, J. Liu and W. Tian, "Study on Surface Corrosion Behavior of Non-Charge-Discharge $LiMn_2O_4$ in $LiPF_6$-based Electrolyte," *International Journal of Electricalchemical Science,* vol. 7, pp. 8299 - 8308 , 2012.

[80] J. -H. Cho and S. T. Picraux, "Silicon nanowire degradation and stabilization during lithium cycling by SEI layer formation," *Nano Letters,* vol. 14, no. 6, pp. 3088-3095, 2014.

[81] X. Wang, F. Fan, J. Wang, H. Wang, S. Tao, A. Yang, Y. Liu, H. B. Chew, S. X. Mao, T. Zhu and S. Xia, "High damage tolerance of electrochemically lithiated silicon," *Nature Communications,* vol. 6, p. 8417, 2015.

[82] Q. P. McAlliester, K. E. Strawhecker, C. R. Becker and C. A. Lundgren, "In situ atomic force microscopy nanoindentation of lithiated silicon nanopillars for lithium ion batteries," *Journal of Power Sources,* vol. 257, pp. 380-387, 2014.

[83] B. Hertzberg, J. Benson and G. Yushin, "Ex-situ depth-sensing indentation measurements of electrochemically produces Si-Li alloy films," *Electrochemistry Communications,* vol. 13, pp. 818-821, 2011.

[84] L. A. Berla, S. W. Lee, Y. Cui and W. D. Nix, "Mechanical behavior of electrochemically lithiation silicon," *Journal of Power Sources,* vol. 273, pp. 41-51, 2015.

[85] V. A. Sethuraman, M. J. Chon, M. Shimshak, V. Srinivasan and P. R. Guduru, "In Situ Measurements of Stress Evolution in Silicon Thin Films During Electrochemical Lithiation and Delithiation," *Journal of Power Sources,* vol. 195, no. 15, pp. 5062-5066, 2010.

[86] S. P. V. Nadimpalli, V. A. Sethuraman, G. Bucci, V. Srinivasan, A. F. Bower and P. R. Guduru, "On plastic deformation and fracture in Si films during electrochemical lithiation/delithiation cycling," *Journal of the Electrochemical Society*, vol. 160, no. 10, pp. A1885-A1893, 2013.

[87] G. M. Pharr, T. Y. Tsui, A. Bolshakov and W. C. Oliver, "Effecs of residual stress on the measurement of hardness and elastic modulus using nanoindention," in *MRS Proceedings*, 1994.

[88] I. Yoon, D. P. Abraham, B. L. Lucht, A. F. Bower and P. R. Guduru, "In situ measurement of solid electrolyte interphase evolution on silicon anodes using atomic force microscopy," *Advanced Energy Material*, vol. 6, no. 12, p. 1600099, 2016.